

24 synoptic maps of 296 prominence average magnetic fields measured by Hanle effect during cycle XXI ascending phase

V. Bommier¹, J.L. Leroy², and S. Sahal-Bréchet³

¹ LESIA, Observatoire de Paris, Université PSL, CNRS, Sorbonne Université, Université de Paris, 5 place Jules Janssen, F-92190 Meudon, France

² 65 rue du Château, F-92100 Boulogne-Billancourt, France

³ LERMA, Observatoire de Paris, Université PSL, CNRS, Sorbonne Université, 5 place Jules Janssen, F-92190 Meudon, France

Received ... / Accepted ...

ABSTRACT

Aims. The aim of the present paper is to publish 24 synoptic maps of solar filaments, in which 296 prominence average unambiguous magnetic field vectors were determined by Pic-du-Midi observations between 1974 and 1982, which is the ascending phase of cycle XXI.

Methods. The magnetic field was determined by interpretation of the Hanle effect observed in the He I D₃ line. Previous results about the prominence field polarity and prominence chirality were applied to solve the fundamental ambiguity. The measurements were averaged in each prominence for accuracy reasons.

Results. The result is twofold. First, alternating field directions can be observed from one neutral line to the next one. Second, a general field alignment is found along a solar North-South field distorted under the differential rotation effect.

Key words. Magnetic fields – Polarization – Sun: magnetic fields – Sun: filaments, prominences – Sun: magnetic topology – Sun: surface magnetism

1. Introduction

The first application of the Hanle effect (Hanle 1924, 1991) to solar prominence magnetic fields measurements is due to Hyder in a seminal paper (Hyder 1965), after a theoretical investigation by Öhman (1929), who showed that the radiation emitted by prominences observed at limb should be linearly polarized as due to radiative scattering of the solar incident radiation. As a result, the linear polarization direction should be parallel to the solar limb. But it is not, as observed by Lyot (1934) in the Hydrogen H α line of forty prominences. Further observations of eight prominences also observed in the He I D₃ line (5875.6 Å) are reported by Lyot (1936, 1937). Hyder (1965) summarized all these observations in his Fig. 1, where it can be seen that the linear polarization directions observed by Lyot are rotated with respect to the solar limb. Hyder assigned this rotation of polarization direction to the Hanle effect, as suggested by Öhman (1929). Rotation of the scattering linear polarization direction is one of the main features of the Hanle effect. In his Fig. 2, Hyder (1965) showed in addition that the resulting magnetic field would be consistent with a mainly North-South oriented field distorted under the differential rotation effect. Thus, the prominence mean magnetic field displays a general structure on the Sun, which is the subject of the present paper.

The observations by Bernard Lyot showed that the linear polarization degree of the He I D₃ line is on the order of a few percent. Lyot obtained it with one significant digit. Forty years later, Jean-Louis Leroy undertook new observations of quiescent prominences at Pic-du-Midi with a coronagraph and a polarimeter designed and put into operation by Ratier (1975). The second significant digit of the He I D₃ polarization degree was de-

termined (Leroy et al. 1977). He planned to repeatedly observe the prominence magnetic field, in order to detect eventual cyclic variations. As a result, 379 prominences were observed between 1974 and 1982, which is the ascending phase of cycle XXI.

The first theoretical model of Hanle effect in solar prominences was developed by House (1970a,b). However, the atomic density matrix approach developed by Bommier & Sahal-Bréchet (1978) and Bommier (1980) was first able to perform all the required averages on atoms and incident radiation directions from the underlying solar surfaces. This led to the first Hanle effect diagrams of the He I D₃ line of solar prominences (Sahal-Bréchet et al. 1977). These diagrams form a data basis, in which linear interpolation was applied to determine the 379 prominence magnetic field. For accuracy reasons, only 323 prominences were retained at this step. In six cases, the observed values were not fitted by the diagrams.

However, the obtained magnetic solution is ambiguous. In exact right angle scattering, two field vectors symmetrical with respect to the line of sight are responsible for the same effect on the linear polarization. As a consequence, they remain ambiguous. As discussed in Bommier & Sahal-Bréchet (1978), this ambiguity is to be related to the very large radiation wavelength with respect to the atomic size. When scattering is not exactly at right angle, the two ambiguous solutions may have slightly different field strengths. However the ambiguity is always present. The magnetic field vector is not fully determined as long as the ambiguity is not resolved.

Several methods were developed to solve this fundamental ambiguity. One is comparison of two following days observations. The variation of the scattering angle under the effect of solar rotation modifies the solution symmetry. The method is outlined in Bommier et al. (1981) and the results given in Bommier

Send offprint requests to: V. Bommier, e-mail: V.Bommier@obspm.fr

(2014). The method was also successfully applied by Kalewicz & Bommier (2019) to a prominence more recently observed with spatial resolution with the French THÉMIS telescope settled on the European Izaña site on the Tenerife island (Canary Islands, Spain).

A second method was developed from statistical analysis of the mirror behavior of the ambiguity solution symmetry, together with the previous result of small angle between the field vector and the prominence long axis. This preliminary result was obtained from the Polar Crown prominences of the sample, where the prominence long axis, which is the associated filament main axis, is aligned with the solar parallel and also the line of sight. In this case, the angle between the field vector and the prominence long axis is the same for both ambiguous solutions. This angle was found to be on the order of 25° (Leroy et al. 1983). The statistical analysis of Leroy et al. (1984) showed that the prominence magnetic field vector is mainly of Inverse polarity with respect to the photospheric field neighboring polarities separated by the prominence long axis, which coincides with the photospheric neutral line below the filament.

This result was later on confirmed by comparing the ambiguous solutions issued from two spectral lines of different scattering geometry as a result of different optical thickness. This technique was applied to fourteen prominences observed at Pic-du-Midi in He I D₃, which is optically thin, and in Hydrogen H α , which is not optically thin and where the prominence absorption and internal radiation contribution modify the incident radiation anisotropy and scattering. The Inverse polarity was found in twelve of the fourteen prominences (Bommier et al. 1994).

Another important point is the horizontality of the prominence magnetic field, as shown for the first time by Athay et al. (1983) from the Stokes II spectropolarimeter (Baur et al. 1980, 1981) observations at Sacramento Peak. The horizontality of the prominence magnetic field was later on recovered by Schmieder et al. (2014b) from observations with the THÉMIS telescope (Schmieder et al. 2013, 2014a). This result about the field horizontality was applied to the magnetic field determination in the 323 prominences observed at Pic-du-Midi. The ambiguity was resolved in most of cases by selecting the Inverse polarity solution when the two ambiguous solutions correspond to two different polarities. When this ambiguity resolution method failed, in a smaller number of cases, the ambiguity was resolved by selecting the solution following the chirality law as obtained by Martin et al. (1994). This law is dextral chirality in the northern hemisphere and sinistral chirality in the southern hemisphere. Zirker et al. (1997) showed that this chirality law is in agreement with the Inverse polarity law for prominences as determined by Leroy et al. (1984). The chirality law was previously obtained at high latitudes by Leroy et al. (1983, see their Fig. 5).

In nine cases of our sample, it was not possible to solve the ambiguity neither by the first method nor by the second one. In some cases it was not possible to identify the filament associated to the prominence. As a result, we finally determined unambiguous average field vectors in 296 prominences. In the present paper, we publish the synoptic maps of the solar filaments (complemented with the photospheric field polarity and neutral line from the McIntosh maps of NOAA/SEC), on which we have reported the 296 prominence average magnetic field vectors. This confirms the large scale structure of the prominence and solar magnetic field, already outlined in Fig. 13 of Leroy et al. (1984).

In the following, we discuss in more details the magnetic field determination method from the measurements in Sect. 2

and we present the measurement results and synoptic maps in Sect. 3. We conclude in Sect. 4.

2. The Hanle effect applied to prominence magnetic field measurements

2.1. The atomic density matrix formalism

The Hanle effect (Hanle 1924, 1991) applies to a spectral line formed by radiative scattering. Except in the case of forward or backward scattering, the line results in being linearly polarized with polarization direction perpendicular to the scattering plane. From this stage, the Hanle effect is characterized by two features, namely a depolarization and a rotation of the polarization direction. It is assigned to the partial destruction by the magnetic field of the atomic coherences, or phase relationships between different sublevel wavefunctions in the excited state. These phase relationships are created by absorption of polarized (or directive) incident radiation (Sahal-Br  chot 1981). However, they are quantitatively described as off-diagonal elements of the atomic density matrix. These off-diagonal elements are called coherences. Those coherences are maximum in zero magnetic field. When the magnetic field separates the sublevels connected by the coherence, it becomes partially destroyed if the period of the magnetic Larmor precession is shorter than the radiative lifetime.

When the Larmor frequency is much higher than the inverse radiative lifetime, the coherences become completely destroyed and the line linear polarization becomes independent of the magnetic field strength. This is the case of the forbidden lines of the Solar Corona where the lifetimes are very long (Sahal-Br  chot 1974, 1977). When $\omega\tau \sim 1$, where ω is the Larmor pulsation, which is $2\pi\nu$ where ν is the Larmor frequency, and τ is the upper level lifetime, more precisely when $0.1 < \omega\tau < 10$, the depolarization is partial and sensitive to the magnetic field strength. This implies that each spectral line has its own sensitivity domain to the field strength. A table of spectral lines and their sensitivities can be found in Sahal-Br  chot (1981, Table I). It can be seen in this Table that the He I D₃ line is sensitive to a field strength of about 6 Gauss. It often happened that the prominence field was found of this order of magnitude, which makes He I D₃ particularly well suited to quantitative prominence magnetic field measurements.

In the general case, the line formation description requires to solve the statistical equilibrium equations for the atomic levels and sublevels. Sahal-Br  chot (1977) introduced the magnetic field level separation and collisional transitions in the statistical equilibrium equations. As coherences were not accounted for, this formalism was only able to deal with the case of the saturated Hanle effect with $\omega\tau \gg 1$, which is the case of the forbidden Coronal lines. The problem was to introduce coherences in the statistical equilibrium. In other words, the problem was to write down the statistical equilibrium equations for the full atomic density matrix. This was the PhD work of Bommier (1977), published in Bommier & Sahal-Br  chot (1978), later on extended to higher fields and level crossings by Bommier (1980).

As the atomic density matrix represents the average atom (Sahal-Br  chot et al. 1998), this formalism enabled for the first time quantitative calculation of solar radiation scattering in prominences because it was able of integration on partially directive incident radiation, which is fully described by the incident photospheric radiation density matrix (Bommier & Sahal-Br  chot 1978). It was then possible to complete the work initiated by House (1970a,b). On this occasion, a sign error in the polarization rotation about the magnetic field was corrected. This

sign error is present in Fig. 7 of House (1970b) and also in Fig. 2 of Hyder (1965).

As the experiment by Jean-Louis Leroy was using a Lyot filter and not a spectrograph, the line profile was not resolved. As the Hanle effect is a level and not a line property, it is constant along the line profile (it is however absent from coherent far wings due to Rayleigh scattering). Therefore line profiles are absent in the above described formalism. After a suggestion by Landi Degl'Innocenti (1983, 1984), the polarized radiative transfer equation was developed for the atomic density matrix. Both system of equations were rederived in the S -matrix formalism by Bommier & Sahal-Br  chot (1991, statistical equilibrium equations) and Bommier (1991, radiative transfer equation). By repelling step by step the Markov approximation, the perturbation development of the matter-radiation interaction was pushed forward and finally added up, which led to the introduction of line profiles and partial redistribution in the formalism (Bommier 1997a,b, 2016).

2.2. Application to the prominence linear polarization

As the two main features of the Hanle effect are depolarization and rotation of the polarization direction, it is usual to characterize the Hanle effect by two parameters, namely the polarization degree p and an angle φ that refers the polarization direction with respect to a reference direction Ox , which is generally the zero-field polarization direction that results from pure radiative scattering.

These two parameters may be related to two of the Stokes parameters (I, Q, U, V). If Ox is the axis of positive Q and is a reference axis perpendicular to the line of sight Oz , p and φ may be related to Q and U by

$$\begin{aligned} p &= \frac{\sqrt{Q^2+U^2}}{I} \\ \cos 2\varphi &= \frac{Q}{\sqrt{Q^2+U^2}} \\ \sin 2\varphi &= \frac{U}{\sqrt{Q^2+U^2}} \end{aligned} \quad (1)$$

It has to be remarked that this equation is able to define φ within π radians or 180° .

Given these two parameters p and φ , it was usual to represent the theoretical Hanle effect by so-called diagrams, which are abaci of the magnetic field effect on linear polarization. Two axes are given in terms of p and φ for vertical and horizontal axis respectively. A given linear polarization (p, φ) is a point in this axis system. Abaci are drawn by plotting those series of points obtained by increasing field strengths with fixed field inclination and azimuth, or by increasing field azimuth for fixed field strength and inclination. Series of abaci are obtained when field inclination is varied. In solar prominence, the field inclination is referred to the local solar vertical axis (the solar radius). An abacus but for pure directive scattering can be found in Fig. 7 of House (1970b). The sign of the polarization rotation is wrong. The first abaci for the solar prominence case in the He I D₃ line, can be found in Sahal-Br  chot et al. (1977). In Fig. 5 of that paper, observation values are also reported as points. This diagram corresponds the the prominence horizontal magnetic field case. It can be seen that the observed values fit very well the theoretical curves, in particular in the central empty space, which is the first indication of horizontal magnetic field in prominences, because those non-horizontal diagrams in Fig. 6 of the same paper do not display such a central empty space. Later on, Bommier (1980) displayed diagrams extended to higher fields and to level-crossings in the He I D₃ line. Similar diagrams can be found in

Landi Degl'Innocenti (1982). A Hanle diagram is the cover illustration of the monograph "Polarization in Spectral Lines" by Landi Degl'Innocenti & Landolfi (2004).

Observation data interpretation is then achieved by performing linear interpolation in diagrams. As two linear polarization parameters are measured when three coordinates of the magnetic field vector are looked for, the field solution is not unique and can be represented as a series (Bommier et al. 1981, Fig. 3). The full determination of the field vector can be achieved by crossing solutions issued from two spectral lines of different sensitivity to the Hanle effect. The He I D₃ line itself is comprised of two fine-structure components, a major one and a minor one. Indeed, the major one is comprised of five unresolved fine-structure components $3d^3D_{3,2,1} \rightarrow 2p^3P_{2,1}$ whereas the minor one is comprised of the single $3d^3D_1 \rightarrow 2p^3P_0$ component. These two components have unequal sensitivity to the Hanle magnetic field as visible in Table I of Sahal-Br  chot (1981). This results from both different lifetime and different Land   factors. As a consequence, they could provide a full magnetic field vector solution. However, they are very close and partially overlap. Their respective observation then requires a spectrograph as was the Stokes II instrument (Baur et al. 1980, 1981). Notwithstanding the problem to separate these two components for polarization analysis, Athay et al. (1983) and Querfeld et al. (1985) were able to determine the full field vector in thirteen and two prominences respectively. They showed that the magnetic field is mainly horizontal in prominences.

The Pic-du-Midi data reported in this paper were on the contrary observed through a Lyot filter. The two components were then not resolved and only two parameters were measured, which are the full line linear polarization degree and direction. The above result of horizontal magnetic field in prominences was then applied for analysis. At the end of the observation campaign, the polarimeter was modified to quasi-simultaneously observe the Hydrogen H α and H β lines. By using both He I D₃ and Hydrogen H β , Bommier et al. (1986) were able to find again nearly horizontal magnetic field vectors in fourteen prominences. Schmieder et al. (2014b) confirmed horizontality for the prominence magnetic field from resolved He I D₃ observation interpreted with PCA analysis applied to the polarization profiles (L  pez Ariste & Casini 2002, 2003; Casini et al. 2003, 2005, 2009). Further investigations were possible inside the prominence fine structure with a better spatial resolution (Levens et al. 2016a,b, 2017; Schmieder et al. 2017).

The He I D₃ line is absent from the incident photospheric spectrum. As a consequence, there is neither Doppler-dimming nor Doppler-brightening effect in this line and the prominence velocity field may be ignored in the analysis, which simplifies the problem and yet increases the interest of this line.

3. Measurement results in 296 prominences

From our full sample of 3297 measurements achieved in 379 quiescent prominences observed in He I D₃ at the Pic-du-Midi during the ascending phase of Cycle XXI (1974-1982), we discarded those prominences for which the identification of the neutral line is doubtful (64 prominences). Several scattered and surprisingly rather uniform recordings were made in each prominence as represented in Fig. 1 of Leroy et al. (1977), through a 5 arcsec wide pinhole. However, the different measurements in each prominence were finally averaged for accuracy reasons. We have discarded those measurements that were not precise enough (inaccuracy larger than 5×10^{-3} for the average linear polarization degree or 10° for the average linear polarization direc-

tion). The result is a unique determination of the average magnetic field vector of 296 quiescent prominences corresponding to 2390 measurements. As explained above, the inversion was obtained by linear interpolation in the horizontal field diagram (Fig. 5 of Sahal-Br  chot et al. 1977, later on extended to higher field strengths). In six cases only the observation fell outside of the diagram. Recent observations with a better spatial resolution (Schmieder et al. 2014b; Levens et al. 2016a,b; Kalewicz & Bommier 2019) display a rather homogeneous magnetic field across quiescent prominences, so that the consideration of their average field makes sense.

The object of the present paper is to plot those average prominence magnetic field vectors in synoptic maps of the solar filaments. Indeed, a prominence is a filament observed at limb. A filament is a stretched structure along a neutral line of the photospheric magnetic field. This neutral line separates the positive photospheric polarity from the negative one. We used the 1974-1982 synoptic maps prepared at the Meudon Observatory by M.J. Martres and I. Soru-Escaut, and we complemented them with the magnetic information, neutral lines and photospheric polarities, from the McIntosh maps (NOAA/SEC). These synoptic maps are provided on Figs. 1-24. Each synoptic map displays the whole solar surface observed close to the disk center and the central meridian throughout one full solar rotation, which is 27.28 days long on average. The Carrington longitude is the horizontal axis and the solar latitude is the vertical axis of the plot. The photospheric magnetic field neutral lines taken from the McIntosh maps are added as green lines, and the photospheric magnetic field polarities also taken from the McIntosh maps are referred to with plus (for positive polarity) and minus (for negative polarity) signs on both sides of the neutral lines.

However, the magnetic field solution is ambiguous, as already discussed. In a first step the ambiguity was removed in all cases where the two ambiguous solutions have opposite polarities, by selecting the inverse polarity solution following Leroy et al. (1984). We call this method the polarity method. The polarity of the prominence magnetic field is determined with respect to the neighboring photospheric field polarities. The polarity method enabled the ambiguity resolution for 264 of the full sample of 296 prominences. As the two ambiguous solutions are nearly symmetrical with respect to the line of sight, the method fails when the neutral line lies along a meridian because, in this case, the two ambiguous solutions have the same polarity. As observed by Zirker et al. (1997), most of these 264 prominences, where the polarity method successfully applies, are found to also obey the chirality law of Martin et al. (1994). This law is dextral chirality in the northern hemisphere and sinistral chirality in the southern hemisphere. Therefore, in a second step the ambiguity was removed for the 32 remaining prominences where the polarity method does not apply, by applying the chirality law instead. The chirality law was previously obtained at high latitudes by Leroy et al. (1983, see their Fig. 5).

As the two ambiguous solutions are nearly symmetrical with respect to the line of sight, the chirality method fails when the neutral line lies along a parallel, and the polarity method fails when the neutral line lies along a meridian. Where one of the two methods fails, the other method applies. Thus, both methods are complementary, and in those cases where both methods apply, they give results in agreement for nearly all the cases. However, it must be emphasized that the chirality method is derived from the results of the polarity method. Also, by using this procedure, a few normal polarity prominences were derived by using the chirality method, and, accordingly, a few prominences are found not to obey the chirality law, by using the polarity method to

solve the ambiguity. Such exceptions are preferentially found at places where the general direction of a neutral line is changing.

As a result, we obtained unambiguous average horizontal magnetic field vectors of 296 prominences each associated to a filament observed eight days before (W limb) or after (E limb). We reported these vectors in the synoptic maps of Figs. 1-24. The magnetic field vector, one for each prominence, is reported as a red or orange arrow of length $2 \log B$, in order to better see the weaker fields and avoid too long arrows. The B value, expressed in Gauss, has always been found above one. Thus, $\log B$ with B in Gauss is always nonzero and positive. At the top-left corner of each plot, the red arrow represents $2 \log B$ for $B = 10$ Gauss and is provided as a reference unit. In the maps, the arrow is in red when the ambiguity is resolved by applying the polarity method. The arrow is in orange when the ambiguity is resolved by applying the chirality method.

Two main features may be seen through those 24 maps. First, alternating field directions can be seen from one neutral line to the next one, as for instance in Figs. 12, 17, 20. This was schematized in Fig. 5 of Leroy et al. (1983). Second, the field vectors are generally aligned with a solar North-South field distorted under the differential rotation effect. This differential rotation effect was already pointed out by Hyder (1965, Fig. 2), but with a sign error about the field direction. The cyclic variation may be observed along these 24 maps. The Polar Crown belt is formed in 1978 (see Fig. 12), raises in latitude and disappears at pole in 1982 in Fig. 22. This cyclic behavior was already summarized in Fig. 13 of Leroy et al. (1984).

4. Conclusion

We publish these 24 synoptic maps of disambiguated averaged horizontal magnetic field vectors in 296 filament/prominences in order to present with details what was already synthesized in Fig. 5 of Leroy et al. (1983) and Fig. 13 of Leroy et al. (1984), namely: 1/ alternating field directions from one neutral line to the next one; 2/ general field alignment along a solar North-South field distorted under the differential rotation effect, as already observed by Hyder (1965, Fig. 2). The small angle between the field vector and the prominence long axis appears as systematic and could also result from the differential rotation effect, following also Fig. 13 of Leroy et al. (1984). The average value of this angle is 43° (see the angle histogram in Bommier & Leroy 1998, Fig. 1).

At the end of the observing period, the Pic-du-Midi polarimeter was able to observe quasi-simultaneously the He I D₃ and Hydrogen H β lines. Four polarization parameters were then measured, namely two polarization degrees and two linear polarization directions. Three of them correspond to the determination of the full magnetic field vector, whose horizontality was verified in fourteen prominences. The remaining fourth parameter corresponds to the determination of an additional parameter, which was the electron density responsible for line depolarisation by collisions. The density was found to be on the order of $1 \times 10^{10} \text{ cm}^{-3}$, which is one order of magnitude weaker as generally believed from Stark effect analysis. Besides, Stehl   et al. (1983) showed that the quasistatic approximation usually applied to the Stark effect modeling is probably responsible for electron density overestimation. They showed that results in better agreement with ours are obtained when ion dynamics is accounted for in the Stark effect modeling.

Upon concluding, we would like to emphasize how important is to identify the observed prominence with a filament ob-

served on the disk some days before or after, in order to properly evaluate the average scattering angle of the photospheric radiation by the prominence. Quiescent prominences are sufficiently high to enable departures of this angle up to 20° from 90° , i.e., from the so-called plane of the sky. It has to be recalled that the linear polarization degree behaves like $\sin^2\theta$, where θ is this angle (Sahal-Bréchet 1974, Eq. (37)). Such a 20° departure is then responsible for a more than 10% relative change of the linear polarization degree, which is of great importance for the accuracy of the magnetic field strength and direction determinations, owing to the nonlinearity of the Hanle effect. This proper determination of the scattering angle from identification of the prominence with a filament is particularly important for Polar Crown prominences, which may even be observed above the Solar Pole. Such identification was not performed by Merenda et al. (2006), who observed a Polar Crown prominence and concluded to non-horizontality of its average magnetic field, contrarily to the general result recalled in the present paper. Their observed polarization was incompatible with the horizontal field Hanle diagram plotted for right-angle scattering, but the scattering angle was not properly evaluated from identification with a filament. The observed polarization was however not so far from the horizontal field Hanle diagram, and the box of measurement inaccuracies was also not plotted, which would have also led to the possibility of average horizontal field in this prominence.

Another important point is the field ambiguity resolution. The magnetic field vector is not fully determined as long as the ambiguity is not resolved. The two ambiguous solutions may be as different as shown in Fig. 1 of Leroy et al. (1984). The lack of ambiguity resolution is frequently masked in the present literature (Schmieder et al. 2013, 2014a,b; Levens et al. 2016a,b) by providing azimuth angle values within 180° for the magnetic field vector. This vector is referred to in spherical coordinates with Oz axis along the local solar radius. The azimuth is then defined from the projection of the magnetic field vector in the horizontal plane, and it is to be within 360° . When the scattering is right angle, the two ambiguous field vectors are symmetrical with respect to the line-of-sight, which is also the reference axis for the azimuth angle definition. The two ambiguous fields then have opposite azimuths. Therefore, only positive azimuths between 0° and 180° are provided in this literature without any ambiguity resolution. Moreover, when the scattering is not at right angle, the two ambiguous solutions are no more exactly symmetrical. Examples may be found in Bommier et al. (1994), where the average field strengths, inclinations and azimuths of the two ambiguous solutions for fourteen prominences are provided in Table III. It can be seen there that the two ambiguous field strengths may differ by a factor up to two, under the effect of the departure from the right angle scattering. This is again an example of the importance of properly evaluating the scattering angle from identification of the observed prominence with a filament observed on the disk some days after or before, as done in the present work. The proper evaluation of the scattering angle enables one of the methods used in the present work for solving the ambiguity, which is to compare the solution pairs obtained on two following days. The solar rotation effect modifies the symmetry of the ambiguous solutions.

References

- Athay, R. G., Querfeld, C. W., Smartt, R. N., Landi Degl'Innocenti, E., & Bommier, V. 1983, *Sol. Phys.*, 89, 3
- Baur, T. G., Elmore, D. E., Lee, R. H., Querfeld, C. W., & Rogers, S. R. 1981, *Sol. Phys.*, 70, 395
- Baur, T. G., House, L. L., & Hull, H. K. 1980, *Sol. Phys.*, 65, 111
- Bommier, V. 1977, *Étude théorique de l'effet Hanle: traitement du cas de la raie D₃ de l'Hélium en vue de la détermination du champ magnétique des protubérances solaires*, Thèse de 3ème cycle (Université Pierre et Marie Curie, Paris 6 University, France)
- Bommier, V. 1980, *A&A*, 87, 109
- Bommier, V. 1991, *Annales de Physique*, 16, 599
- Bommier, V. 1997a, *A&A*, 328, 706
- Bommier, V. 1997b, *A&A*, 328, 726
- Bommier, V. 2014, in *IAU Symposium*, Vol. 300, *Nature of Prominences and their Role in Space Weather*, ed. B. Schmieder, J.-M. Malherbe, & S. T. Wu, 397–400
- Bommier, V. 2016, *A&A*, 591, A59
- Bommier, V., Landi Degl'Innocenti, E., Leroy, J.-L., & Sahal-Bréchet, S. 1994, *Sol. Phys.*, 154, 231
- Bommier, V. & Leroy, J. L. 1998, in *Astronomical Society of the Pacific Conference Series*, Vol. 150, *IAU Colloq. 167: New Perspectives on Solar Prominences*, ed. D. F. Webb, B. Schmieder, & D. M. Rust, 434
- Bommier, V., Leroy, J. L., & Sahal-Bréchet, S. 1986, *A&A*, 156, 79
- Bommier, V. & Sahal-Bréchet, S. 1978, *A&A*, 69, 57
- Bommier, V. & Sahal-Bréchet, S. 1991, *Annales de Physique*, 16, 555
- Bommier, V., Sahal-Bréchet, S., & Leroy, J. L. 1981, *A&A*, 100, 231
- Casini, R., Bevilacqua, R., & López Ariste, A. 2005, *ApJ*, 622, 1265
- Casini, R., López Ariste, A., Paletou, F., & Léger, L. 2009, *ApJ*, 703, 114
- Casini, R., López Ariste, A., Tomczyk, S., & Lites, B. W. 2003, *ApJ*, 598, L67
- Hanle, W. 1924, *Zeitschrift für Physik*, 30, 93
- Hanle, W. 1991, *Zeitschrift für Physik D Atoms Molecules Clusters*, 18, 5
- House, L. L. 1970a, *J. Quant. Spec. Radiat. Transf.*, 10, 909
- House, L. L. 1970b, *J. Quant. Spec. Radiat. Transf.*, 10, 1171
- Hyder, C. L. 1965, *ApJ*, 141, 1374
- Kalewicz, T. & Bommier, V. 2019, *A&A*, 629, A138
- Landi Degl'Innocenti, E. 1982, *Sol. Phys.*, 79, 291
- Landi Degl'Innocenti, E. 1983, *Sol. Phys.*, 85, 3
- Landi Degl'Innocenti, E. 1984, *Sol. Phys.*, 91, 1
- Landi Degl'Innocenti, E. & Landolfi, M. 2004, *Astrophysics and Space Science Library*, Vol. 307, *Polarization in Spectral Lines* (Kluwer Academic Publishers)
- Leroy, J. L., Bommier, V., & Sahal-Bréchet, S. 1983, *Sol. Phys.*, 83, 135
- Leroy, J. L., Bommier, V., & Sahal-Bréchet, S. 1984, *A&A*, 131, 33
- Leroy, J. L., Ratier, G., & Bommier, V. 1977, *A&A*, 54, 811
- Levens, P. J., Labrosse, N., Schmieder, B., López Ariste, A., & Fletcher, L. 2017, *A&A*, 607, A16
- Levens, P. J., Schmieder, B., Labrosse, N., & López Ariste, A. 2016a, *ApJ*, 818, 31
- Levens, P. J., Schmieder, B., López Ariste, A., et al. 2016b, *ApJ*, 826, 164
- López Ariste, A. & Casini, R. 2002, *ApJ*, 575, 529
- López Ariste, A. & Casini, R. 2003, *ApJ*, 582, L51
- Liot, B. 1934, *Compte Rendus de l'Académie des Sciences*, 198, 249
- Liot, B. 1936, *Compte Rendus de l'Académie des Sciences*, 202, 392
- Liot, B. 1937, *L'Astronomie*, 51, 203
- Martin, S. F., Bilimoria, R., & Tracadas, P. W. 1994, in *NATO Advanced Science Institutes (ASI) Series C*, Vol. 433, *NATO Advanced Science Institutes (ASI) Series C*, ed. R. J. Rutten & C. J. Schrijver, 303
- Merenda, L., Trujillo Bueno, J., Landi Degl'Innocenti, E., & Collados, M. 2006, *ApJ*, 642, 554
- Öhman, Y. 1929, *MNRAS*, 89, 479
- Querfeld, C. W., Smartt, R. N., Bommier, V., Landi Degl'Innocenti, E., & House, L. L. 1985, *Sol. Phys.*, 96, 277
- Ratier, G. 1975, *Nouvelle Revue d'Optique*, 6, 149
- Sahal-Bréchet, S. 1974, *A&A*, 36, 355
- Sahal-Bréchet, S. 1977, *ApJ*, 213, 887
- Sahal-Bréchet, S. 1981, *Space Sci. Rev.*, 29, 391
- Sahal-Bréchet, S., Bommier, V., & Feautrier, N. 1998, *A&A*, 340, 579
- Sahal-Bréchet, S., Bommier, V., & Leroy, J. L. 1977, *A&A*, 59, 223
- Schmieder, B., Kucera, T. A., Knizhnik, K., et al. 2013, *ApJ*, 777, 108
- Schmieder, B., Kucera, T. A., Knizhnik, K., et al. 2014a, *ApJ*, 781, 129
- Schmieder, B., Tian, H., Kucera, T., et al. 2014b, *A&A*, 569, A85
- Schmieder, B., Zapiór, M., López Ariste, A., et al. 2017, *A&A*, 606, A30
- Stehlé, C., Mazure, A., Nollez, G., & Feautrier, N. 1983, *A&A*, 127, 263
- Zirker, J. B., Leroy, J. L., & Gaizauskas, V. 1997, *Sol. Phys.*, 176, 279

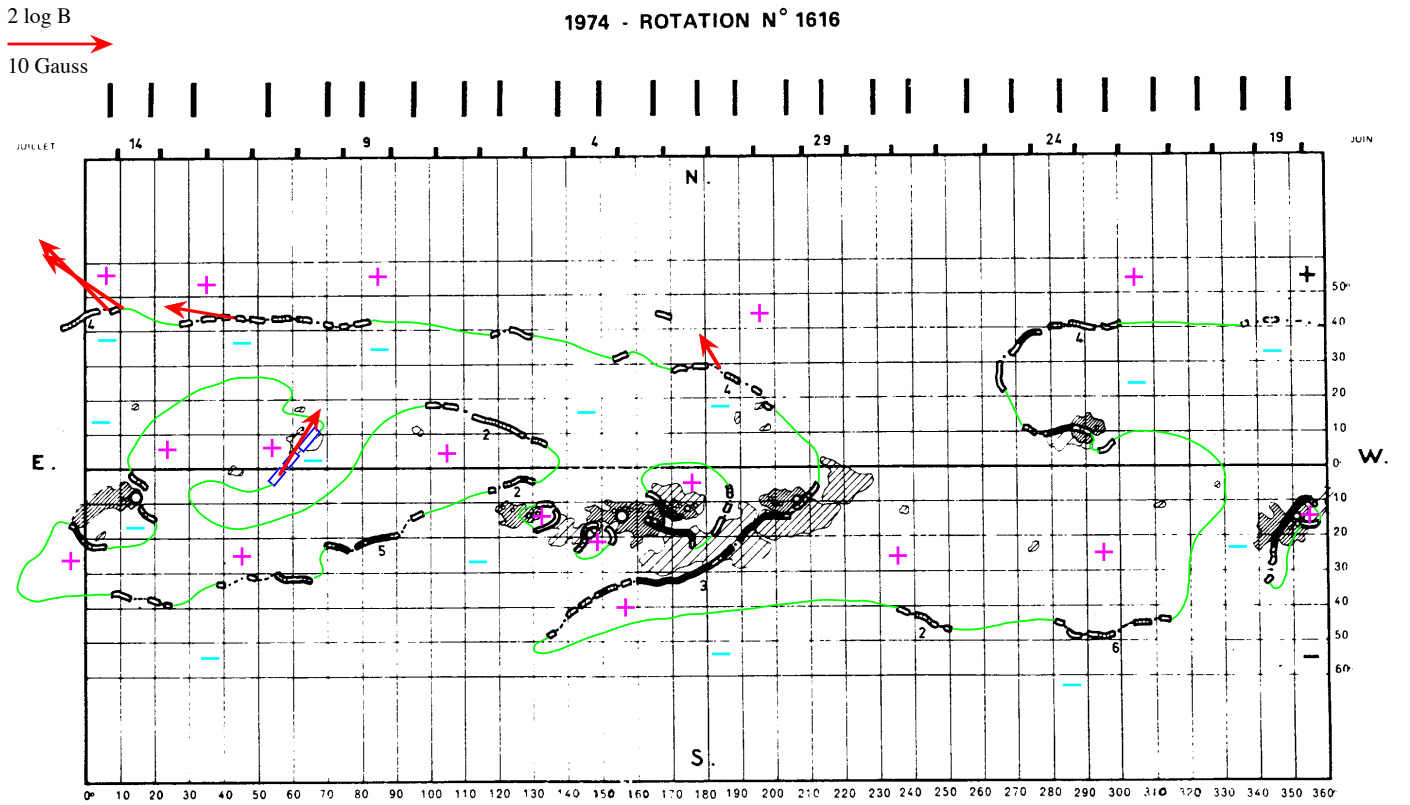


Fig. 1. Synoptic map of rotation 1616. See text about details.

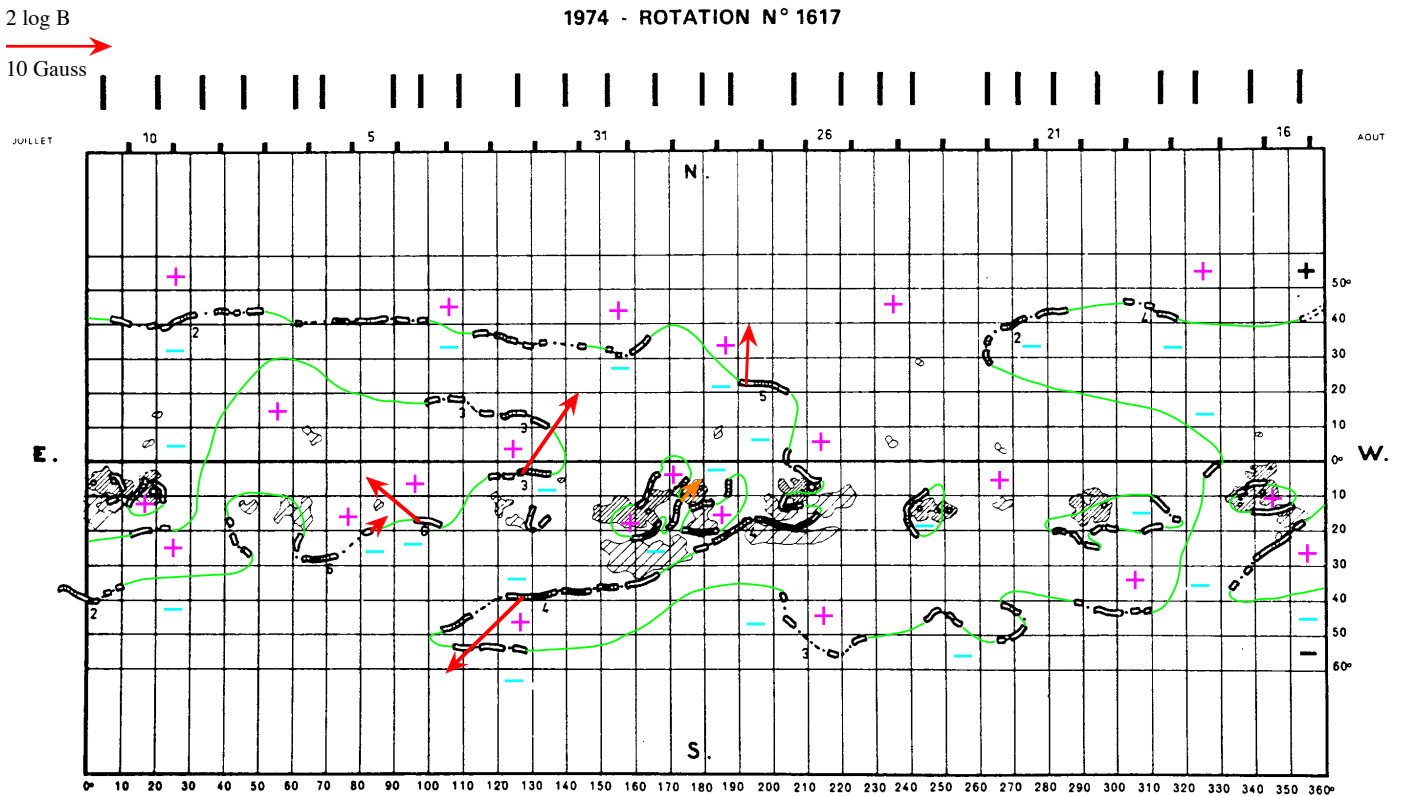


Fig. 2. Synoptic map of rotation 1617. See text about details.

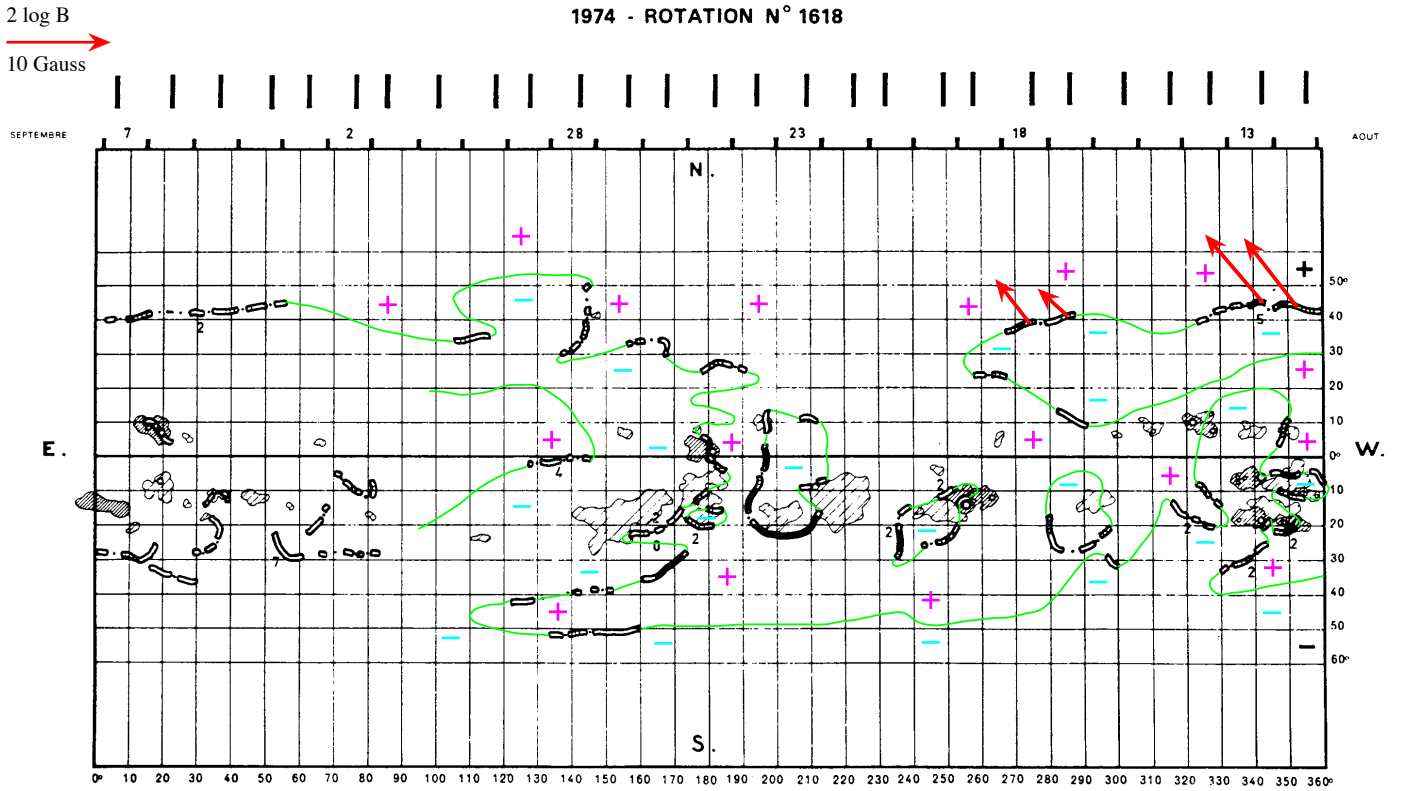


Fig. 3. Synoptic map of rotation 1618. See text about details.

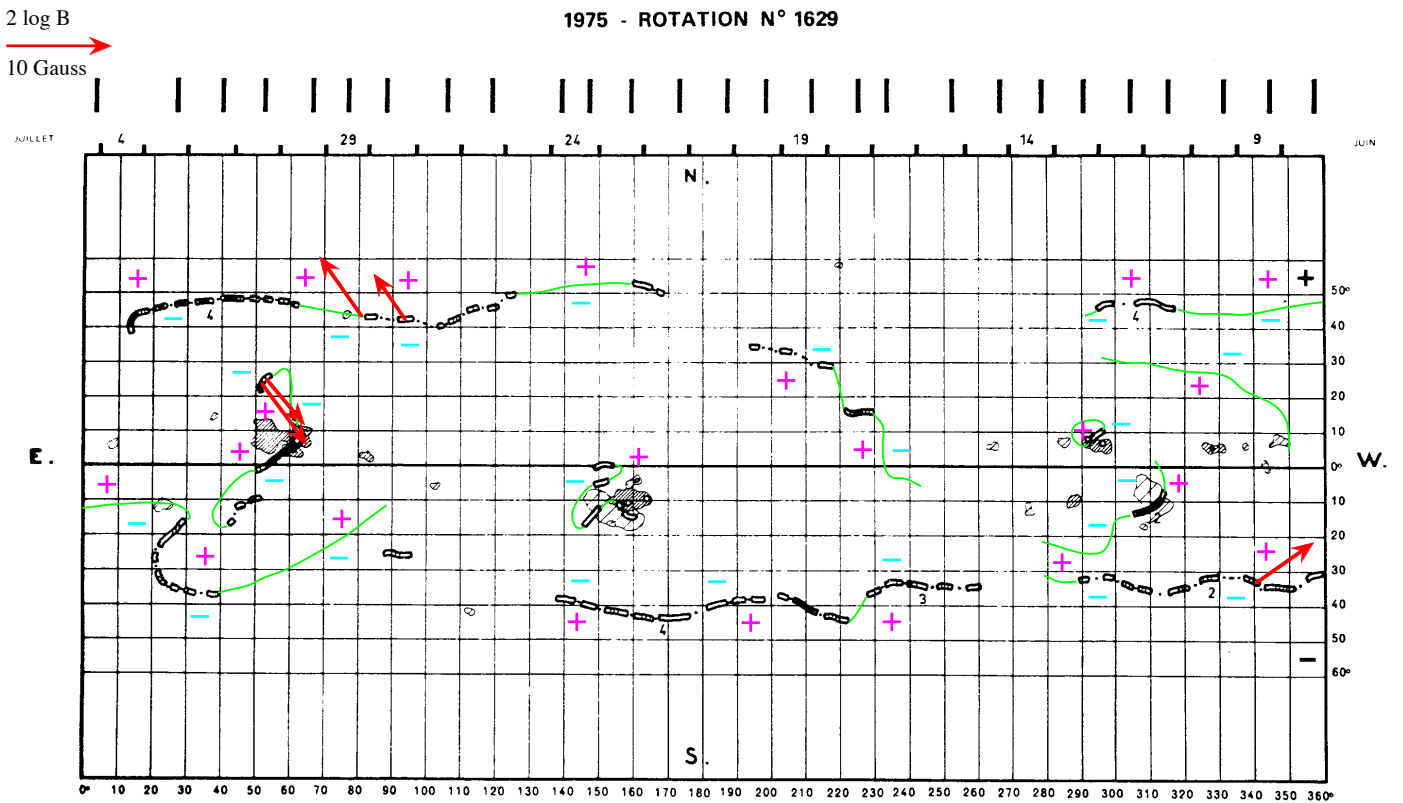
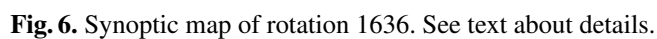
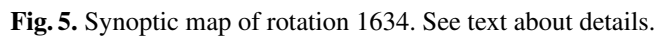


Fig. 4. Synoptic map of rotation 1629. See text about details.



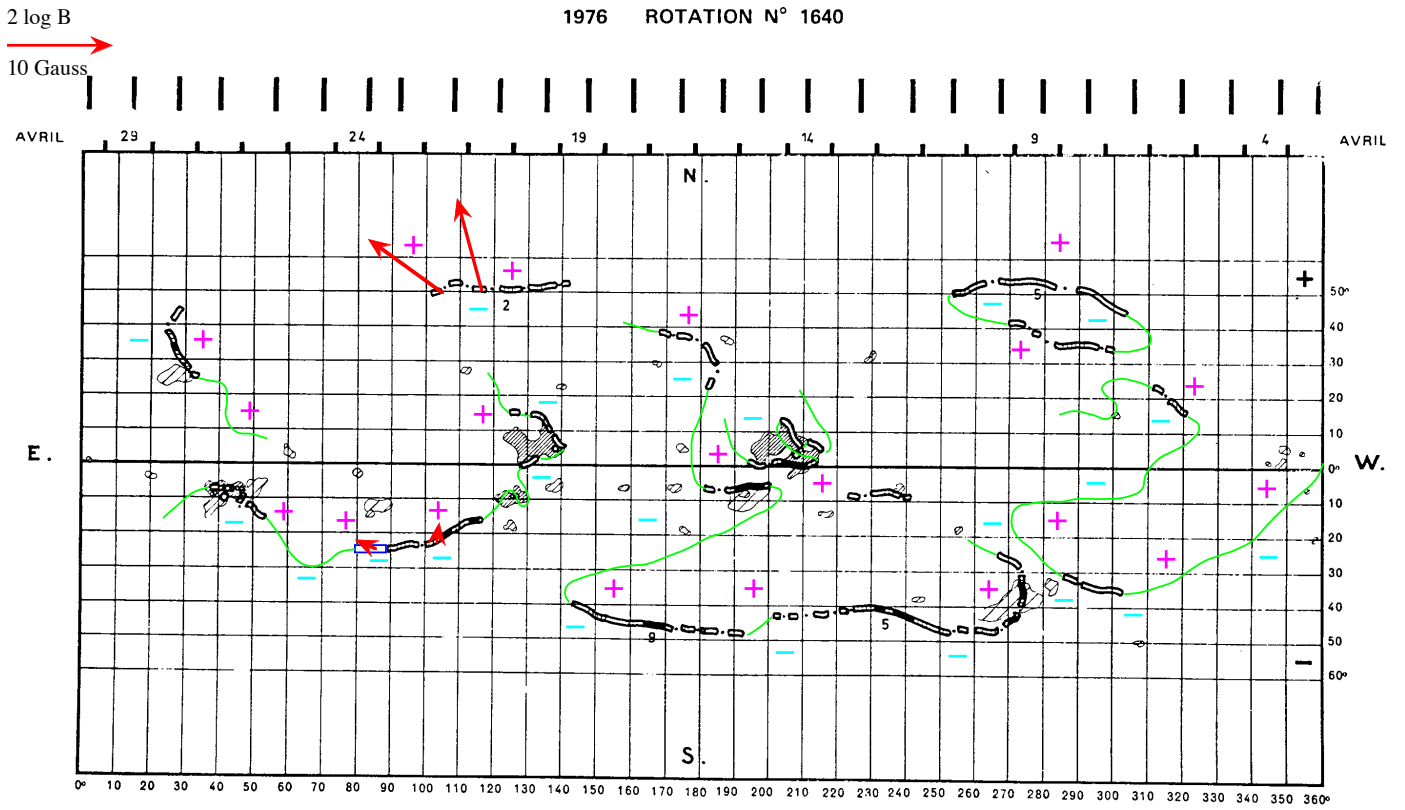


Fig. 7. Synoptic map of rotation 1640. See text about details.

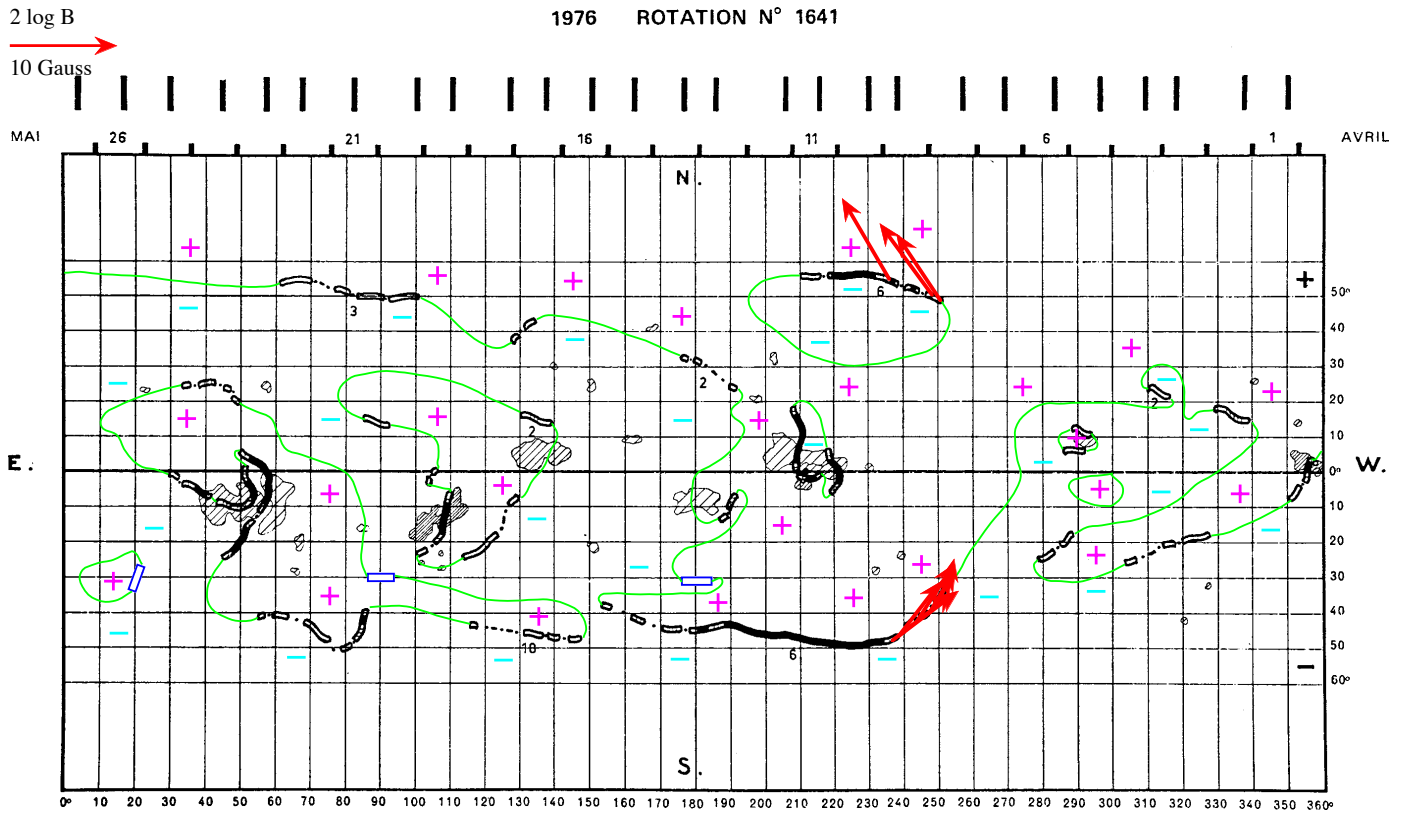


Fig. 8. Synoptic map of rotation 1641. See text about details.

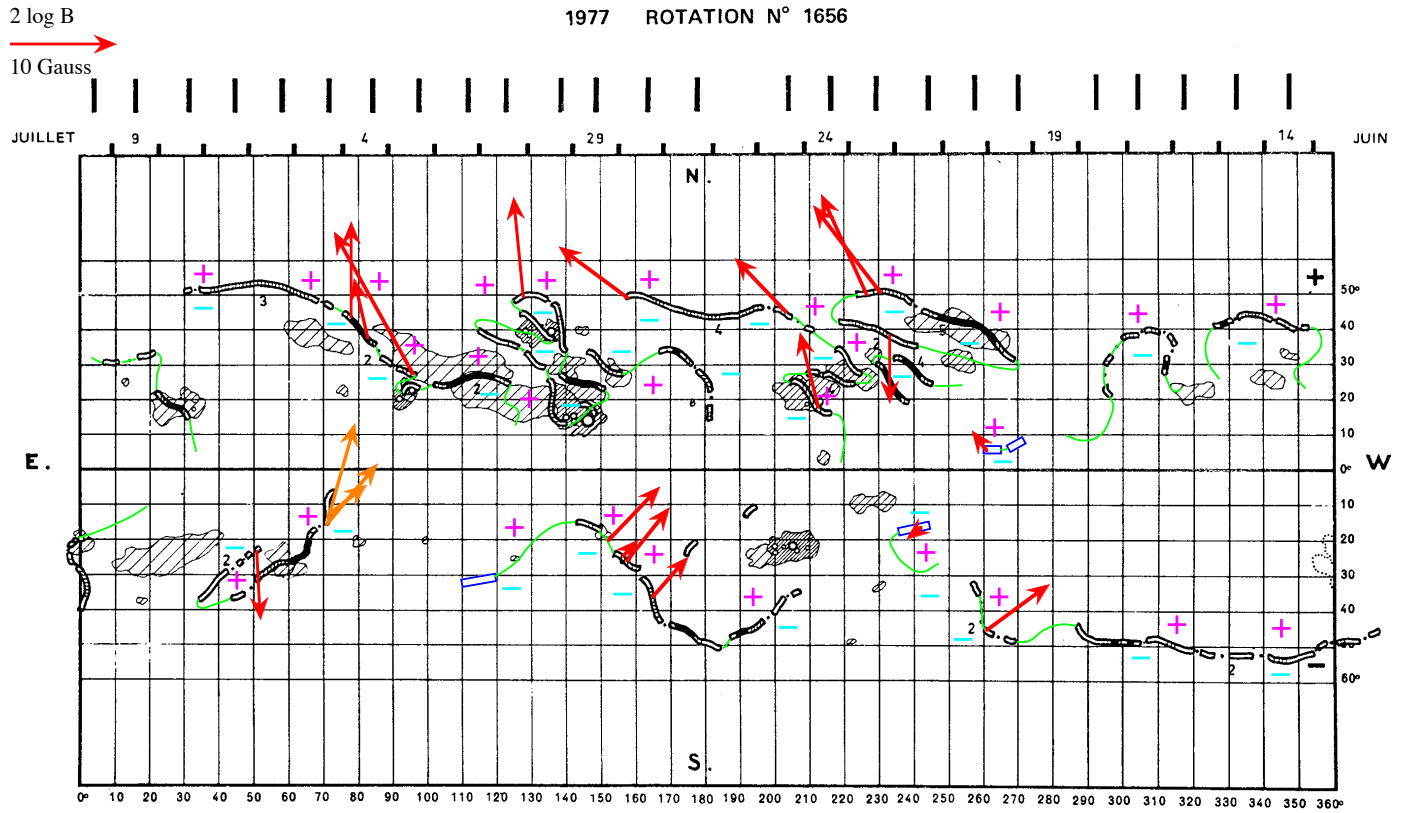


Fig. 9. Synoptic map of rotation 1656. See text about details.

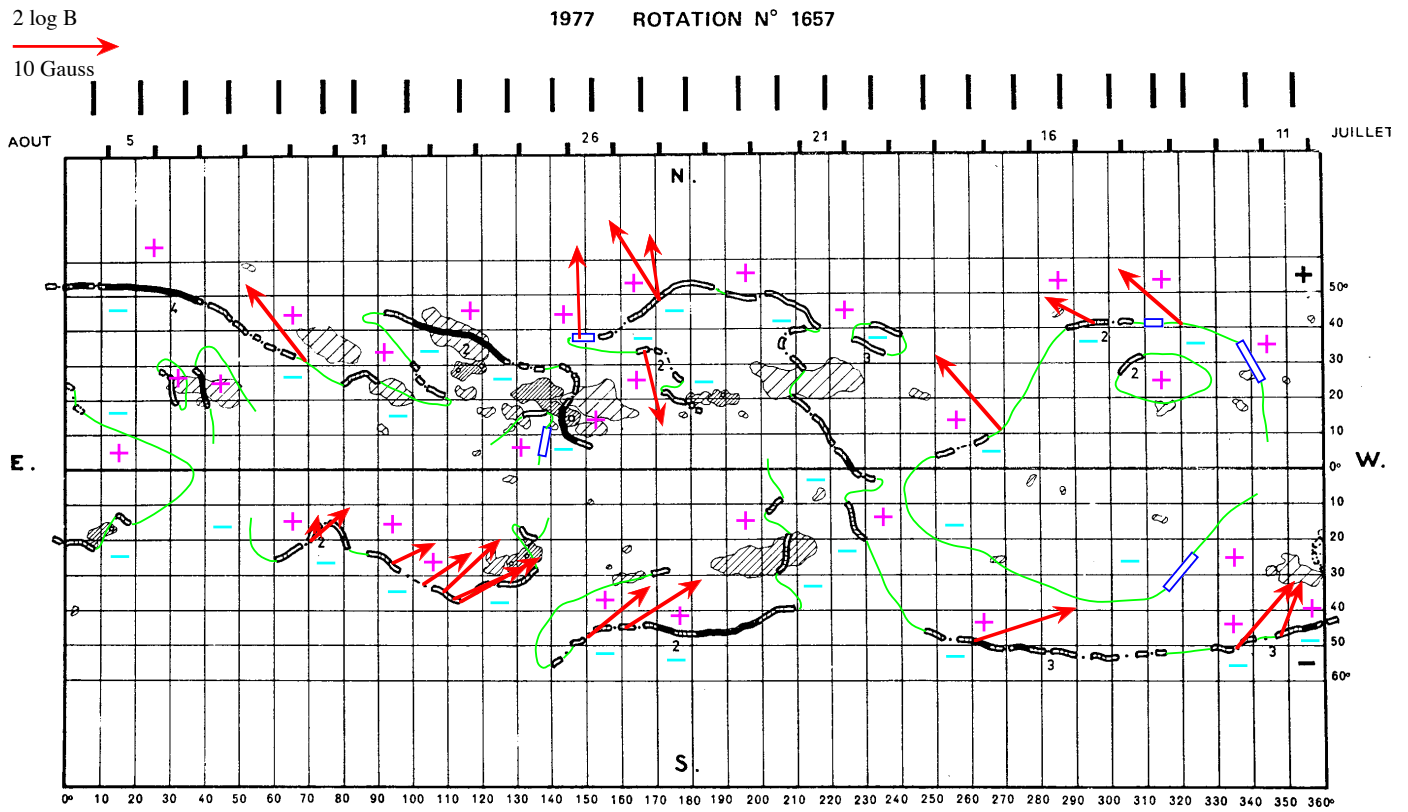


Fig. 10. Synoptic map of rotation 1657. See text about details.

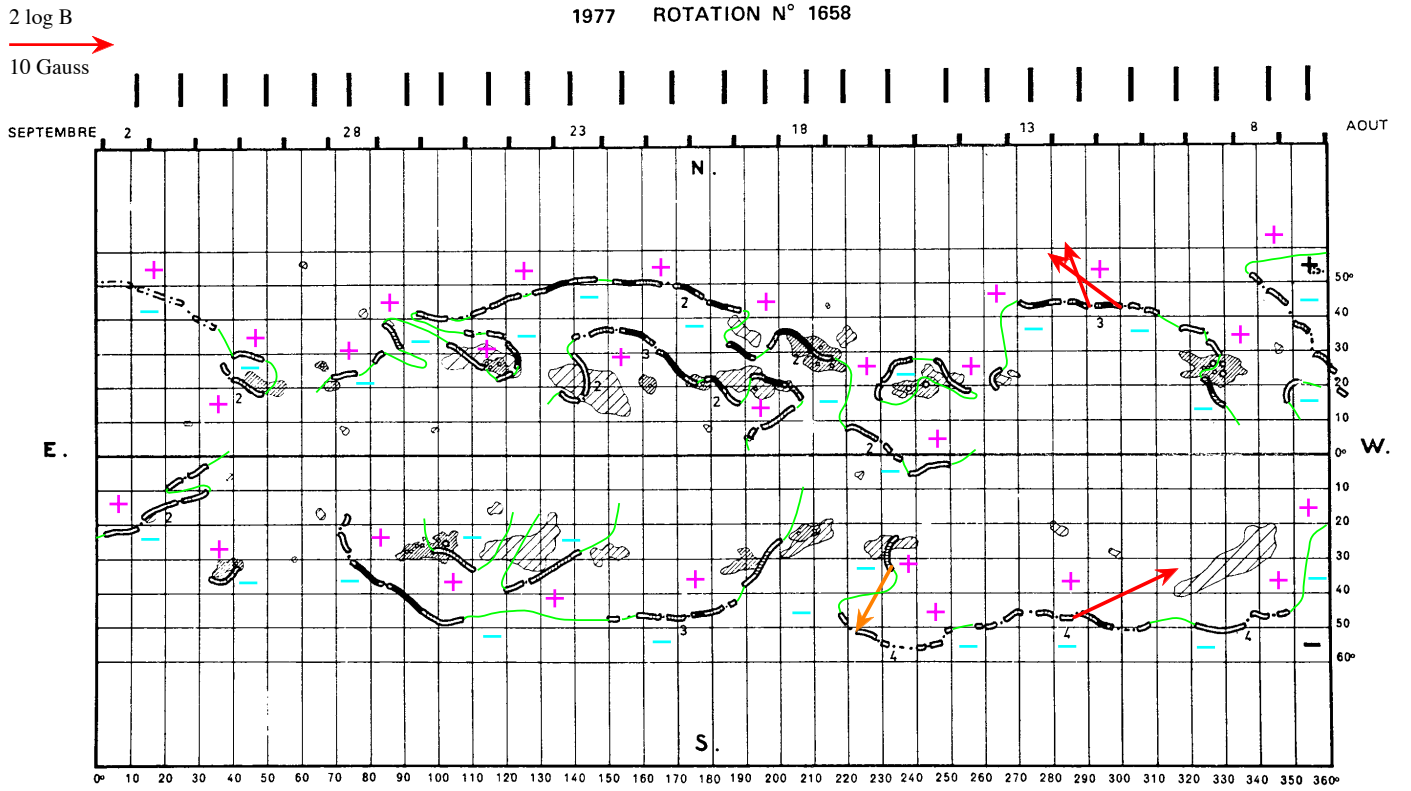


Fig. 11. Synoptic map of rotation 1658. See text about details.

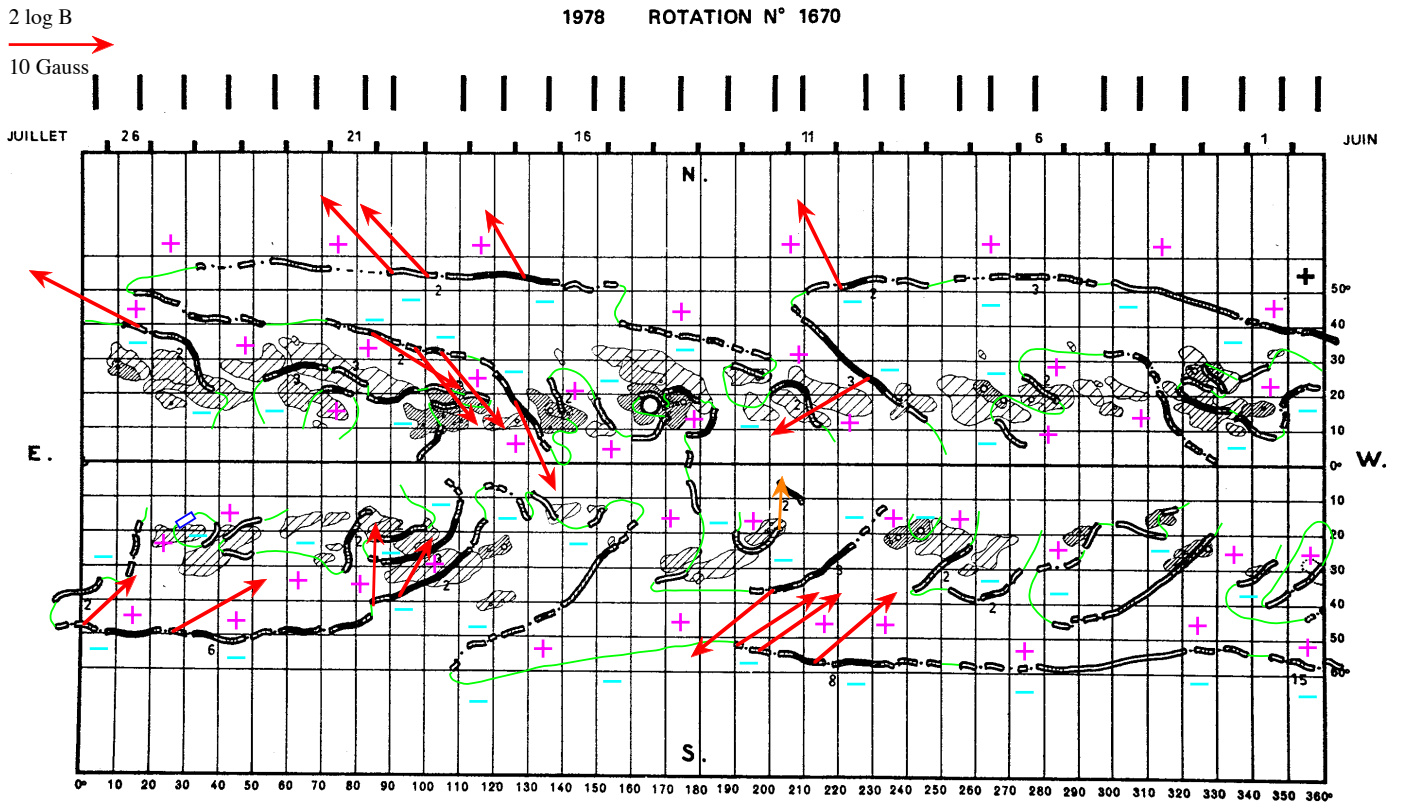


Fig. 12. Synoptic map of rotation 1670. See text about details.

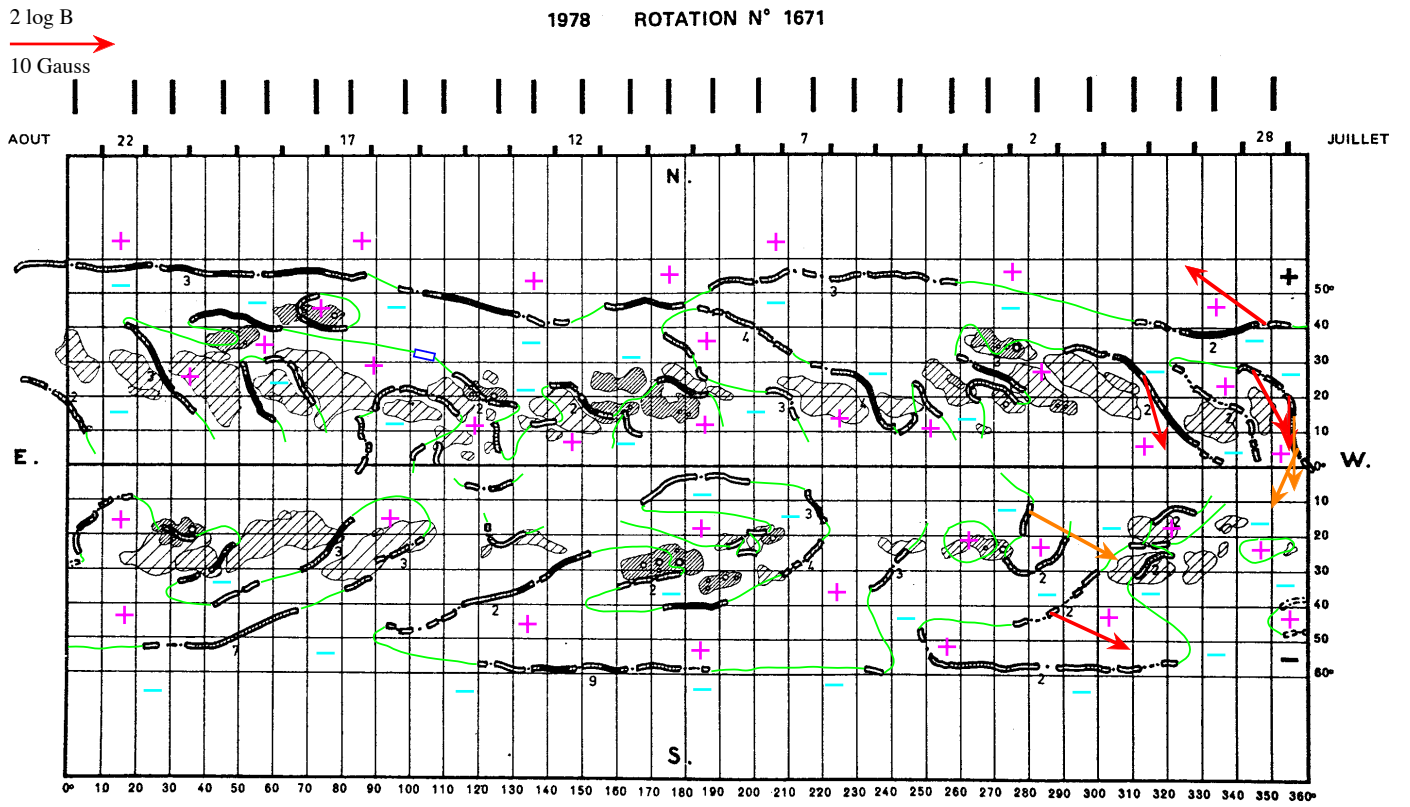


Fig. 13. Synoptic map of rotation 1671. See text about details.

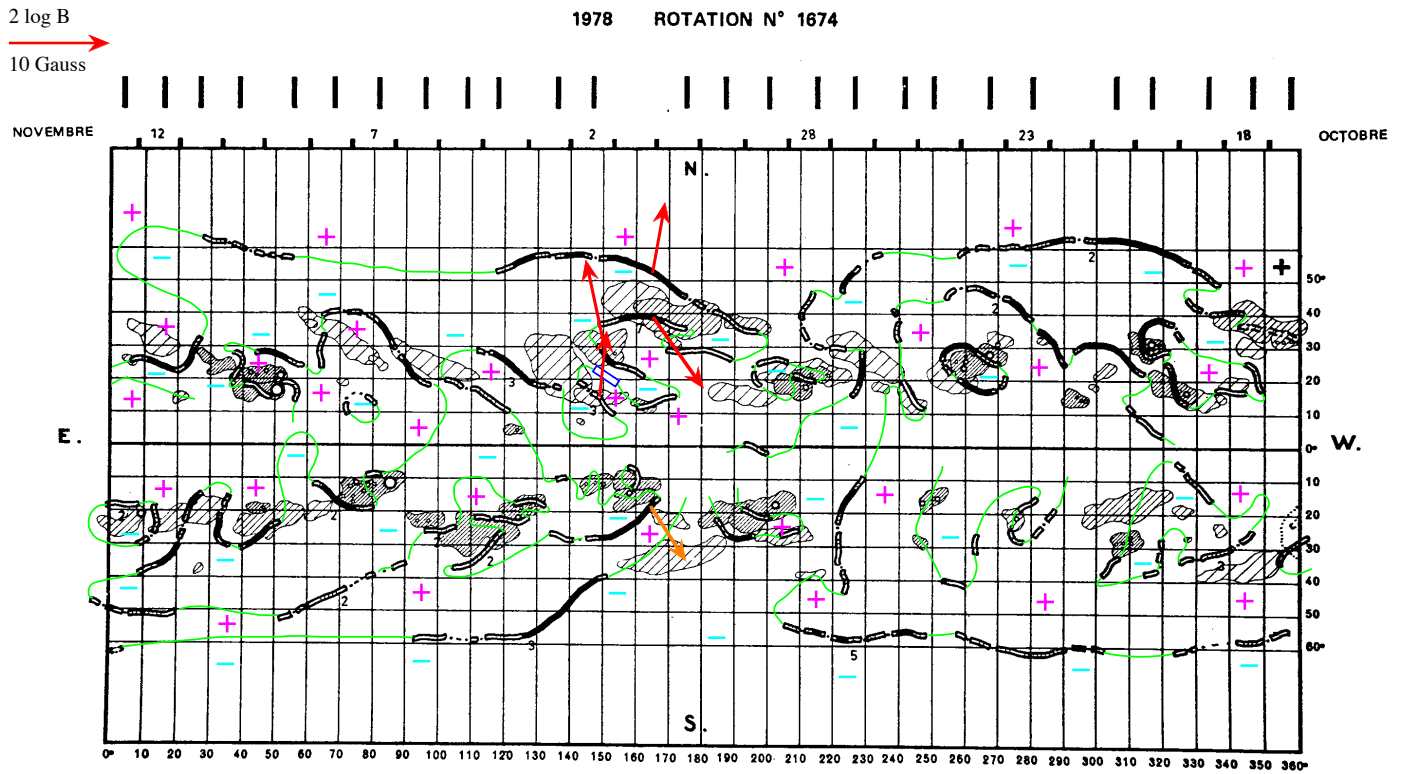


Fig. 14. Synoptic map of rotation 1674. See text about details.

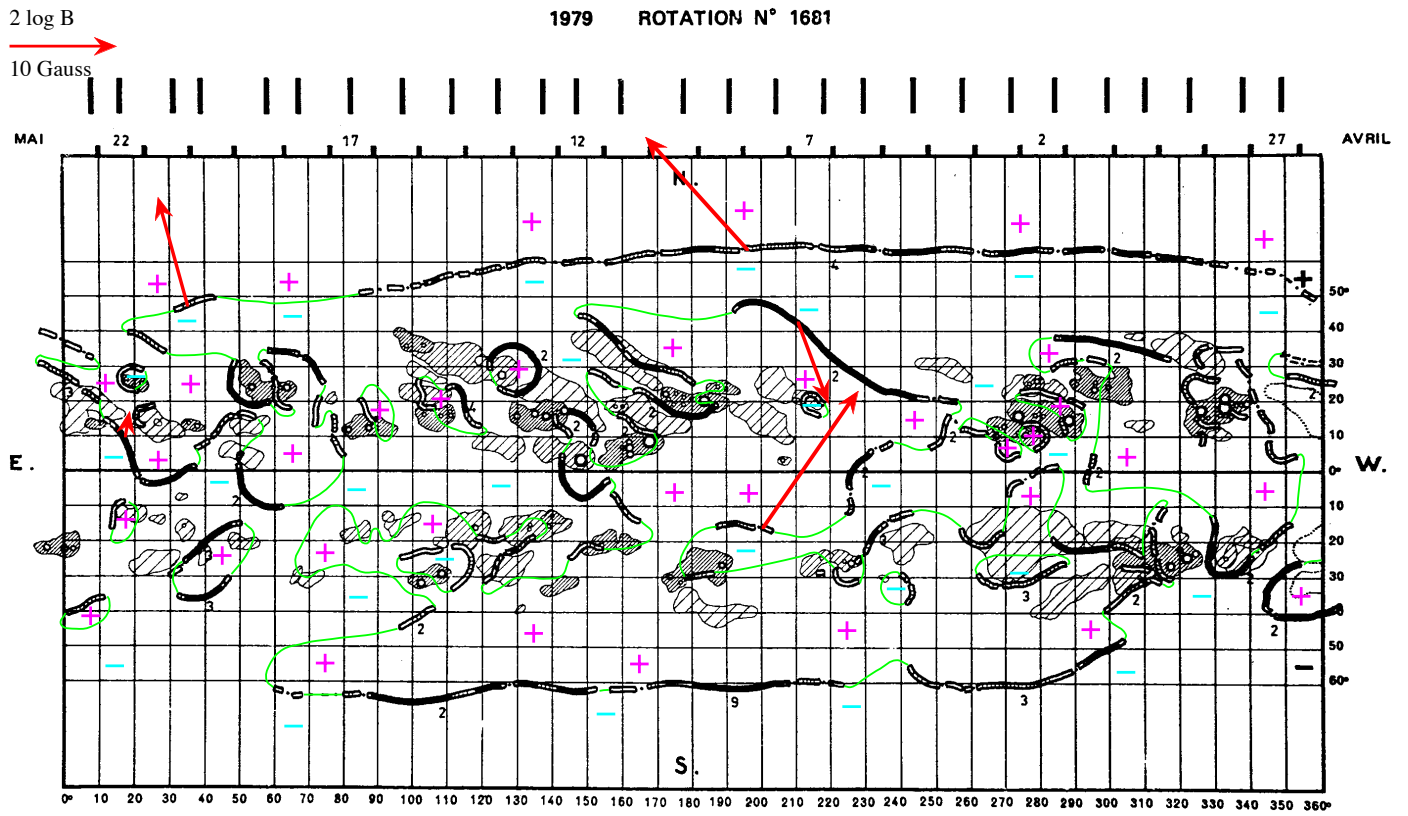


Fig. 15. Synoptic map of rotation 1681. See text about details.

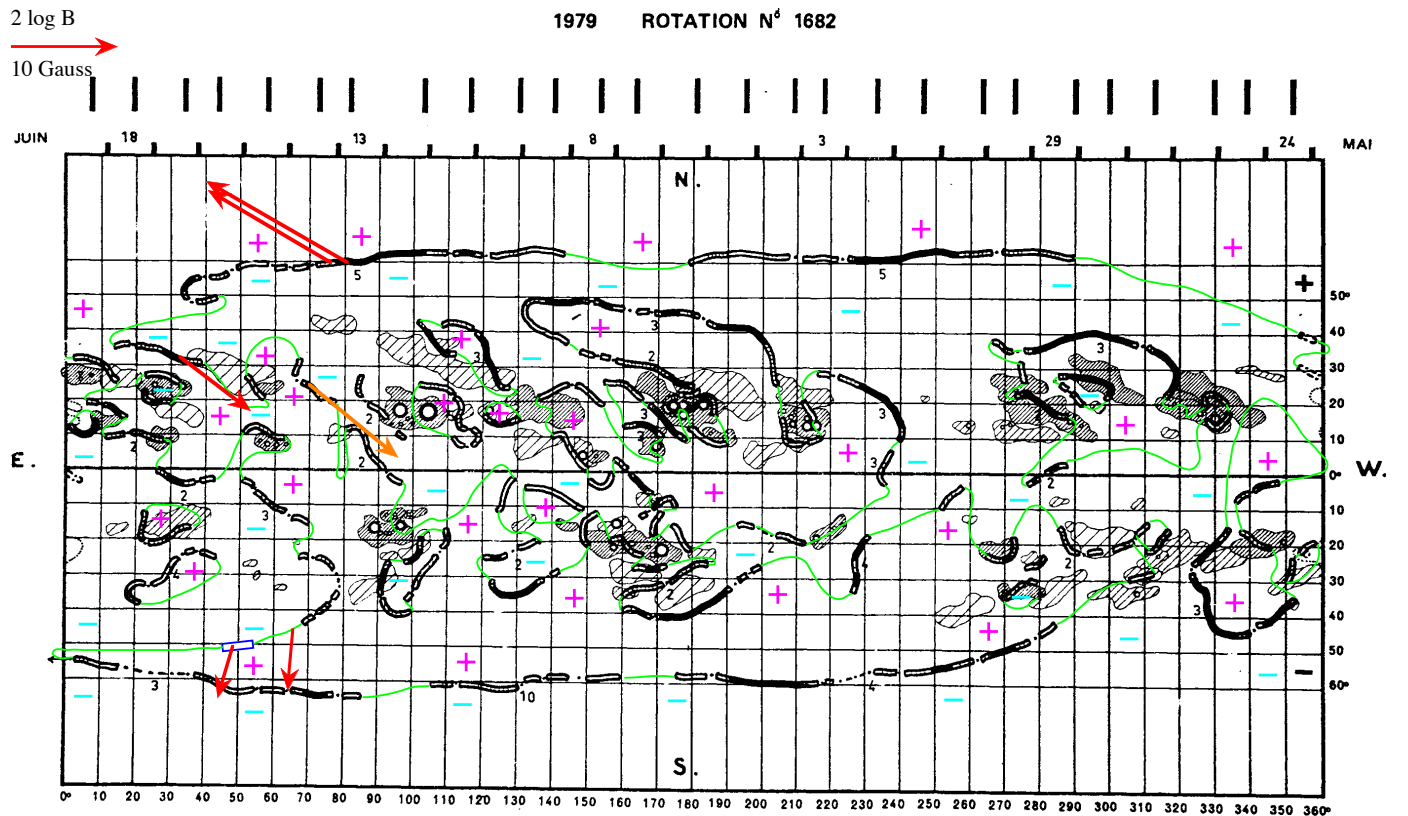


Fig. 16. Synoptic map of rotation 1682. See text about details.

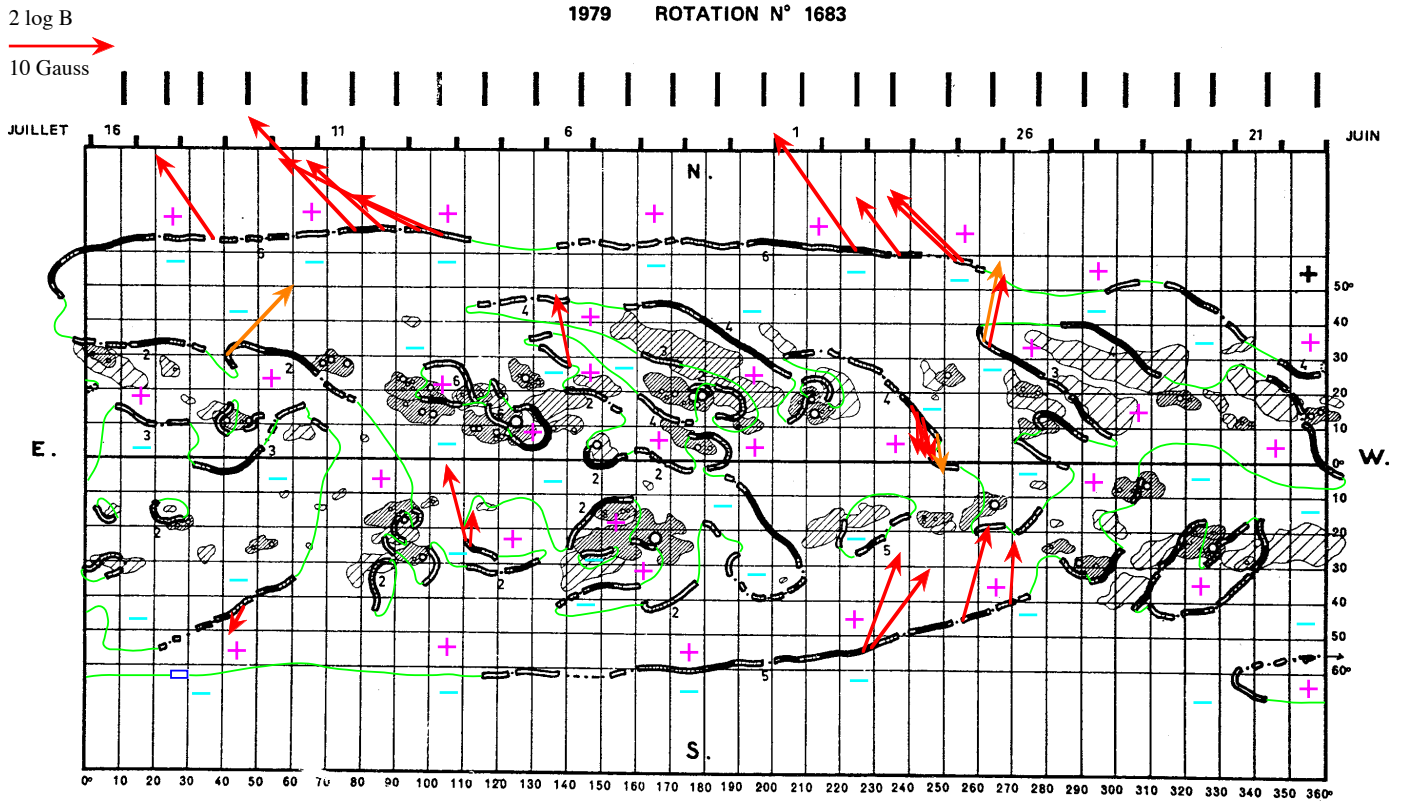


Fig. 17. Synoptic map of rotation 1683. See text about details.

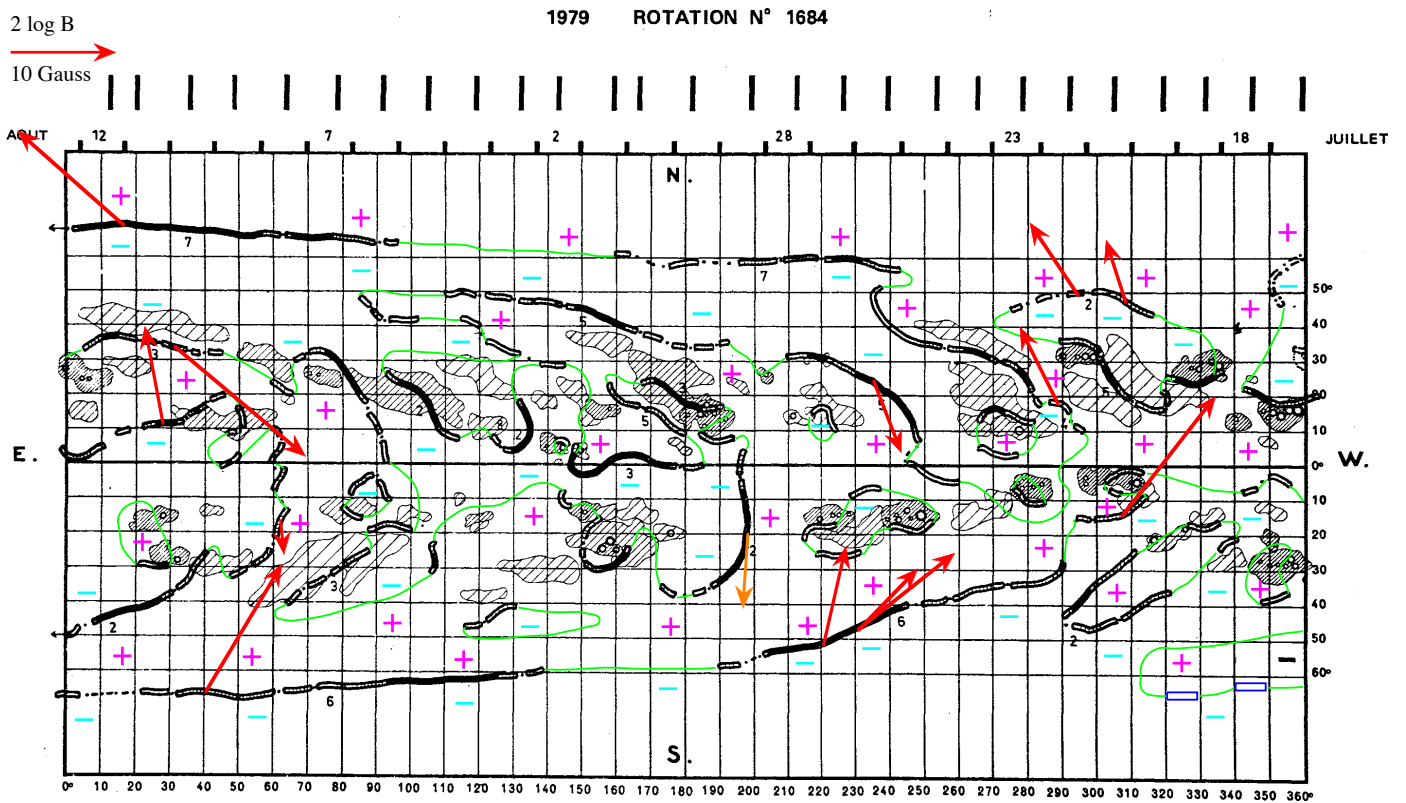


Fig. 18. Synoptic map of rotation 1684. See text about details.

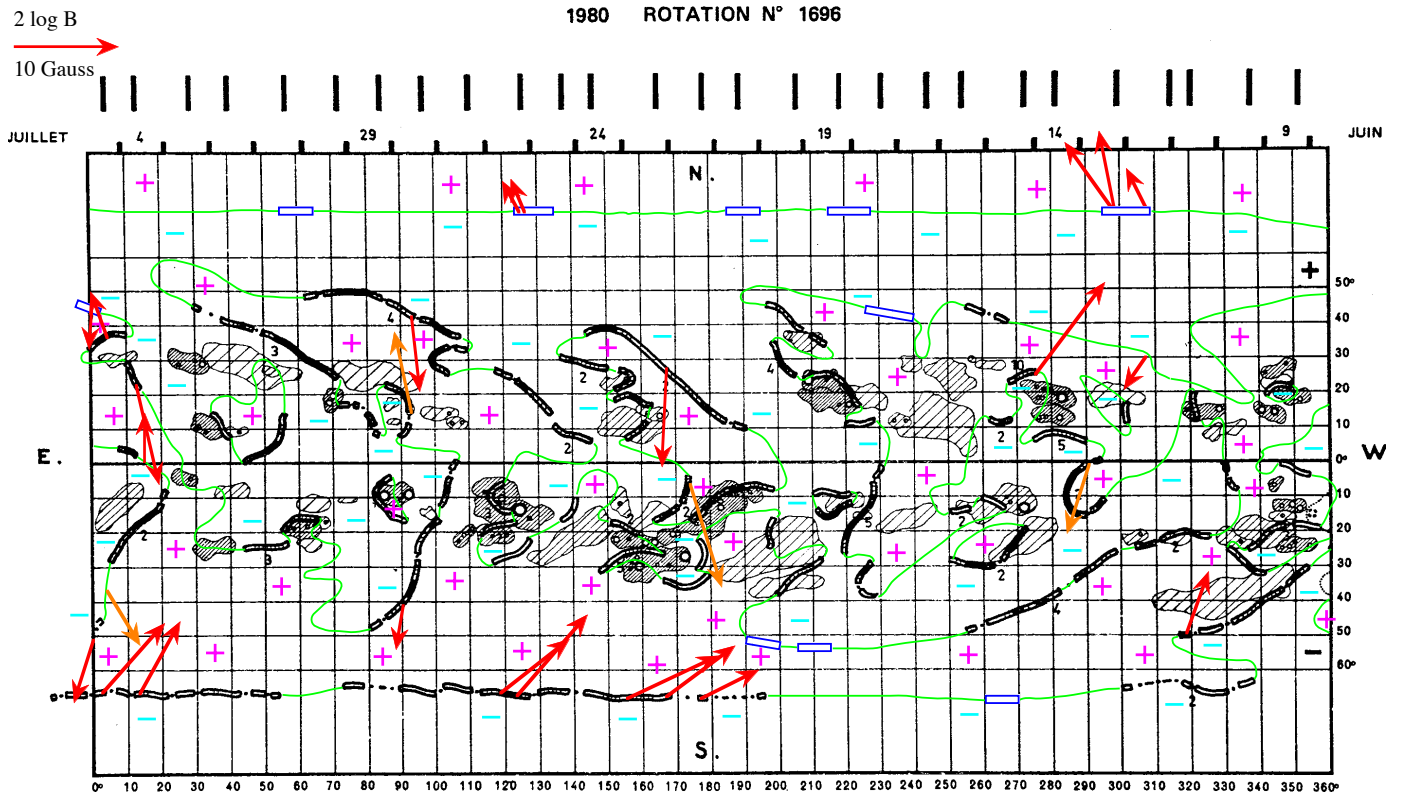


Fig. 19. Synoptic map of rotation 1696. See text about details.

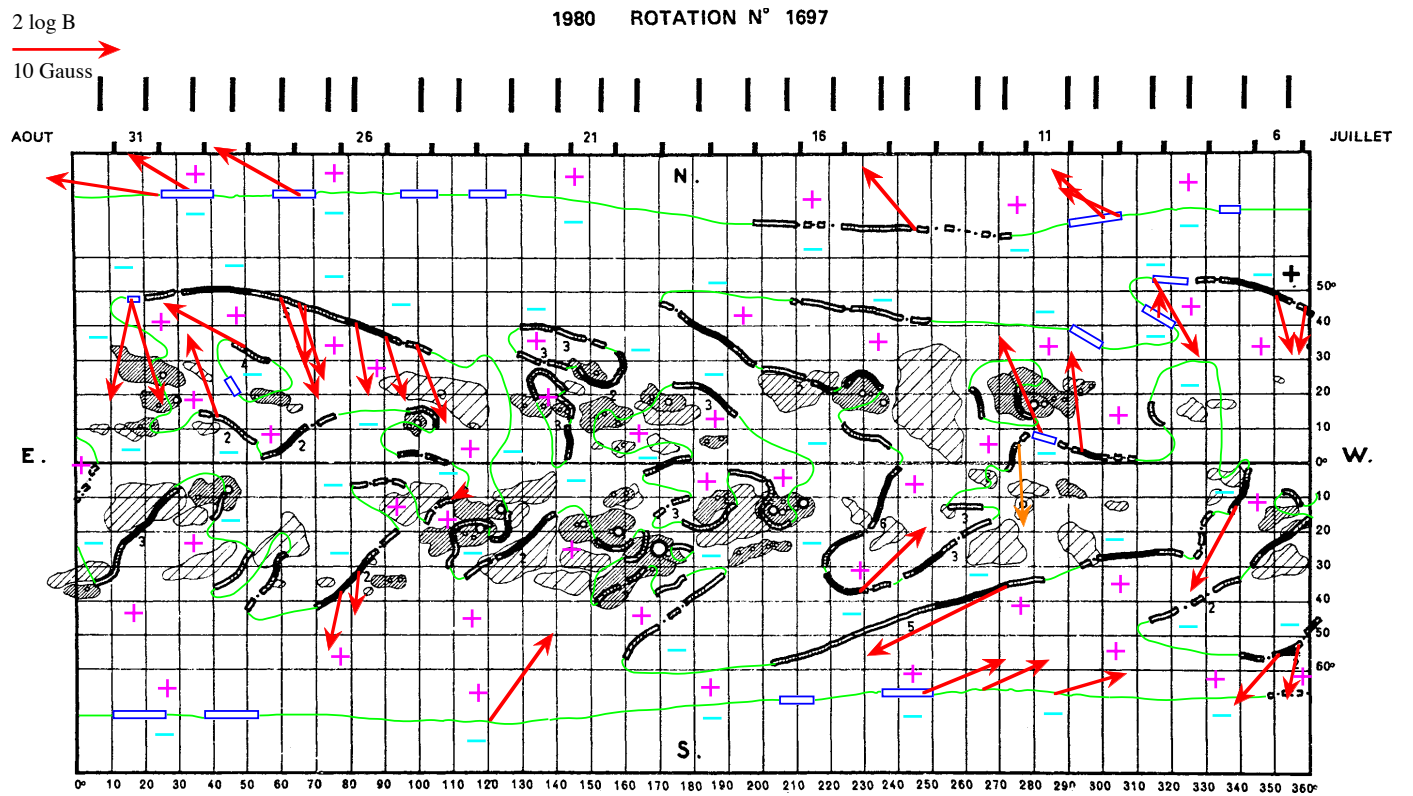


Fig. 20. Synoptic map of rotation 1697. See text about details.

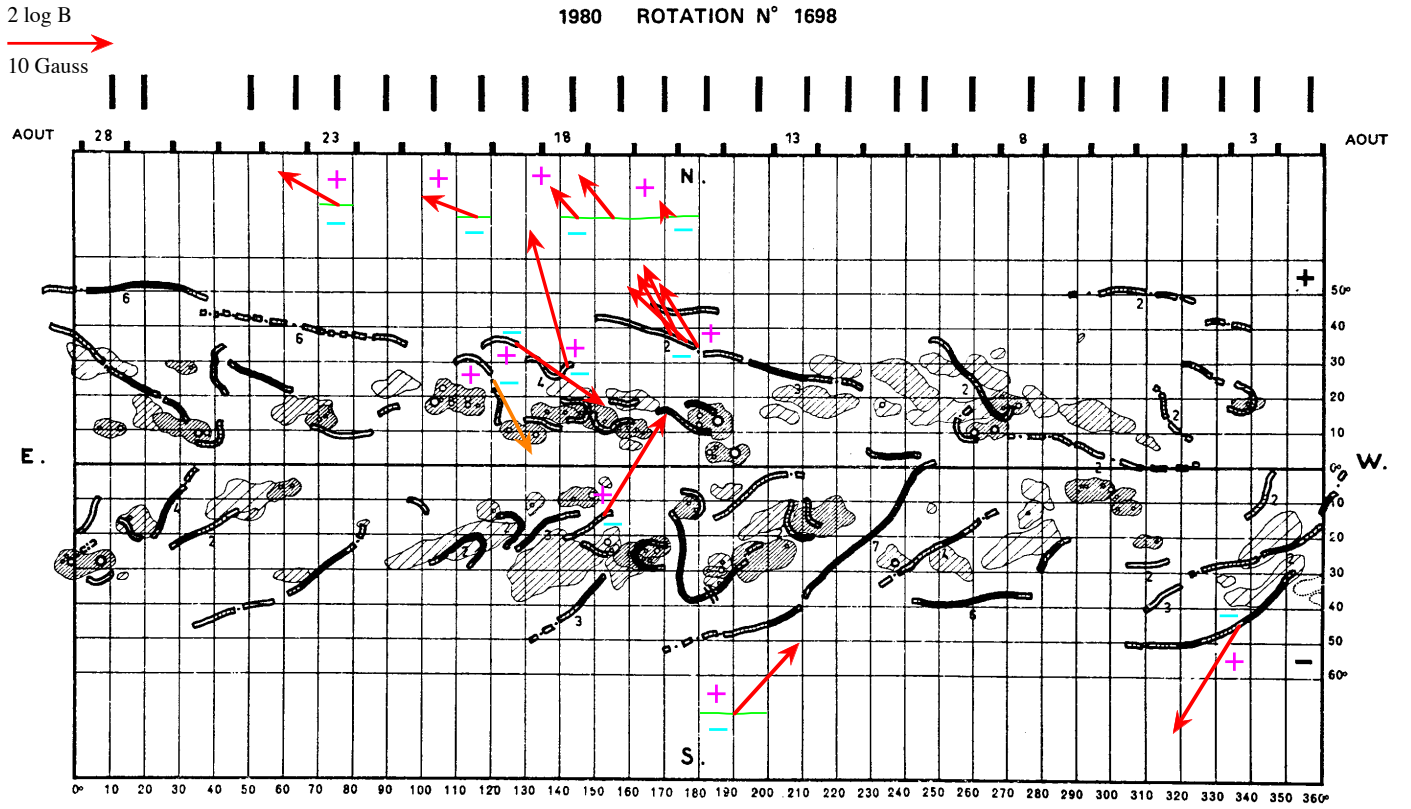


Fig. 21. Synoptic map of rotation 1698
. See text about details.

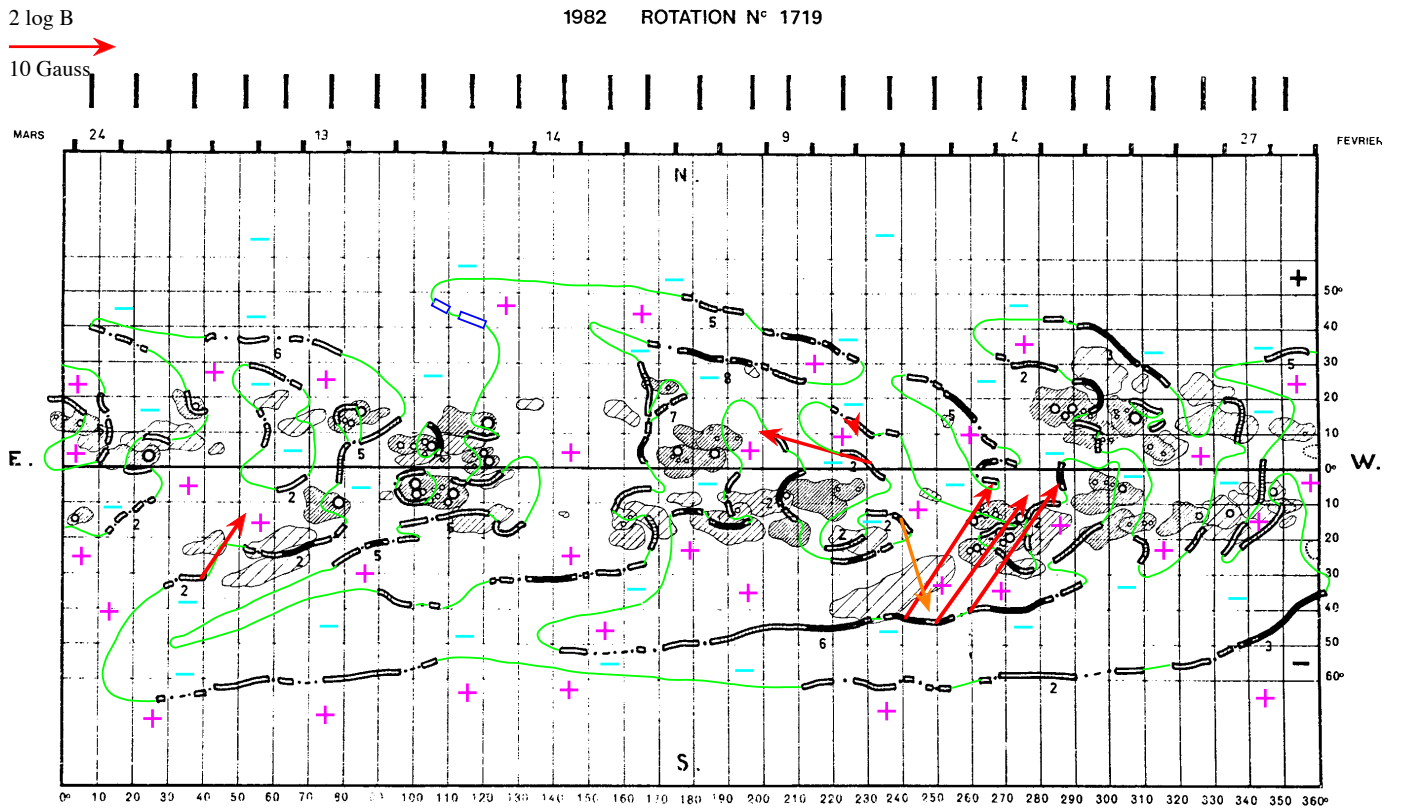


Fig. 22. Synoptic map of rotation 1719. See text about details.

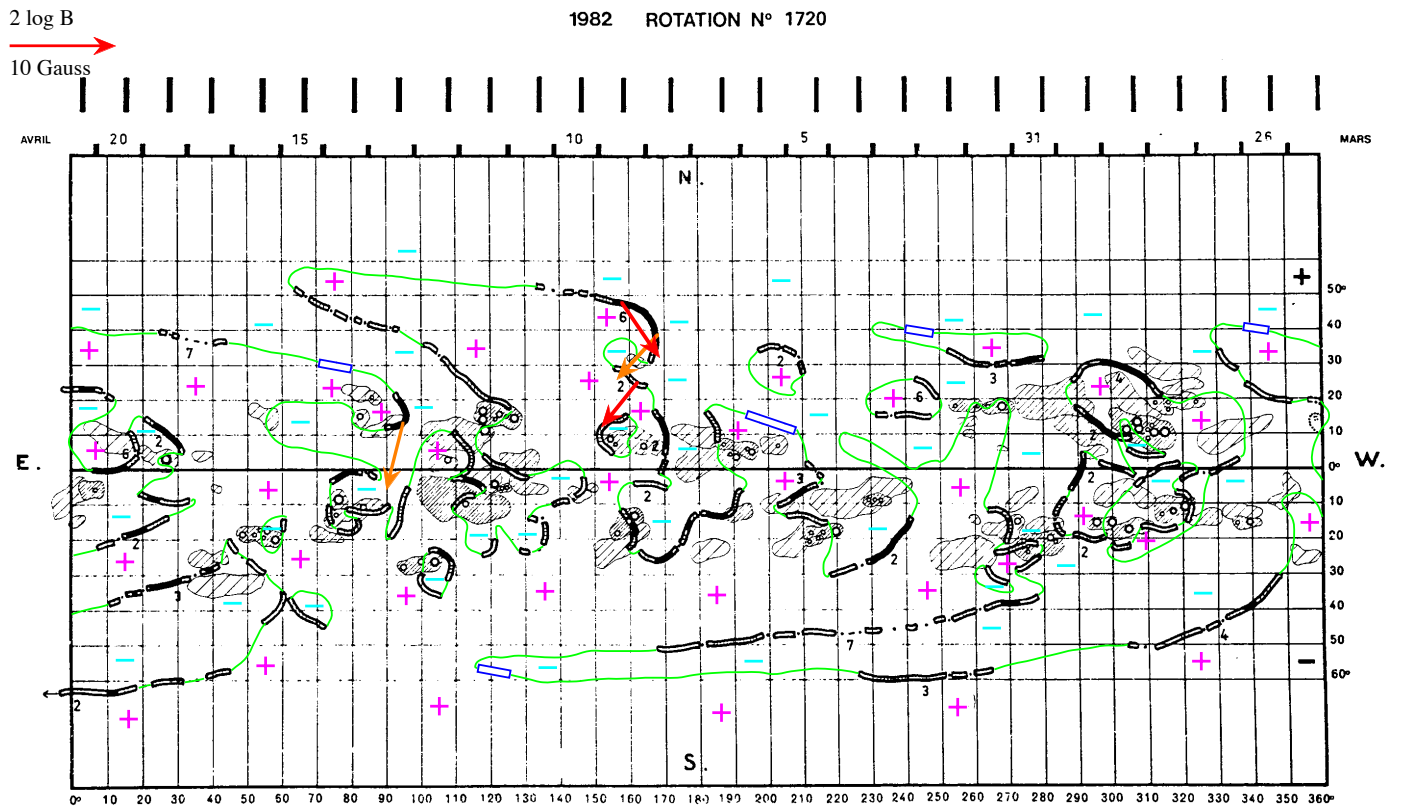


Fig. 23. Synoptic map of rotation 1720. See text about details.

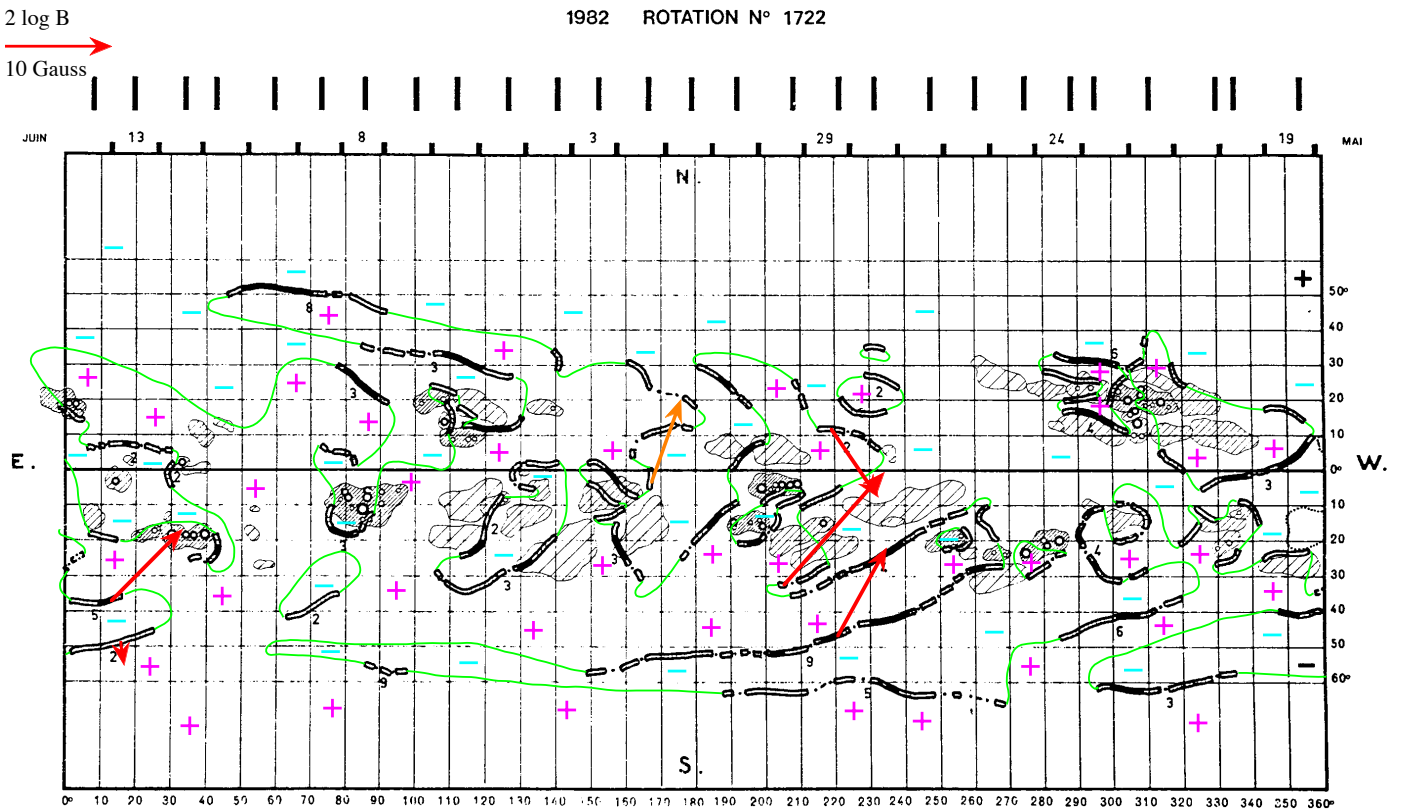


Fig. 24. Synoptic map of rotation 1722. See text about details.